30. Plasmonic Nanomaterials for Nanomedicine

Renat R. Letfullin, Thomas F. George

Plasmonic nanoparticles are being researched as a noninvasive tool for ultrasensitive diagnostic, spectroscopic, and, recently, therapeutic technologies. With particular antibody coatings on nanoparticles, they attach to abnormal cells of interest (cancer or otherwise). Once attached, nanoparticles can be activated/heated with ultraviolet (UV)/visible/infrared (IR), radiofrequency (RF) or x-ray pulses, damaging the surrounding area of the abnormal cell to the point of death. Here, we describe an integrated approach to improved plasmonic therapy composed of nanomaterial optimization and the development of a theory for selective radiation nanophototermolysis of abnormal biological cells with gold nanoparticles and self-assembled nanoclusters. The theory takes into account radiation-induced linear and nonlinear synergistic effects in biological cells containing nanostructures, with focus on optical, thermal, bubble formation, and nanoparticle explosion phenomena. On the basis of the developed models, we discuss new ideas and new dynamic modes for cancer treatment by radiation-activated nanoheaters, which involve nanocluster aggregation in living cells, microbubbles overlapping around laser-heated intracellular nanoparticles/clusters, and the laser thermal explosion mode of single nanoparticles (*nanobombs*) delivered to cells.

30.1 Introduction

In recent years, there has been a tremendous increase in research at the nanoscale for materials (see, for example, [30.1], and references in this handbook). One particular area is the application of plasmonic nanoparticles to enhance the diagnostic and treatment methods available for cancer [30.2–8]. The application of nanotechnology for laser thermal-based killing of abnormal cells (e.g., cancer cells) targeted with absorbing nanoparticles (e.g., gold solid nanospheres, nanoshells or nanorods) is becoming an extensive area of research. Studies have shown that, by coating the surface of nanoparticles with a specific protein (a *targeting agent*, normally an antibody), the nanoparticles will bind to a complementary protein such as found on a cancer cell [30.3, 7–12], as

R. Vajtai (Ed.), *Springer Handbook of Nanomaterials*, DOI 10.1007/978-3-642-20595-8_30,

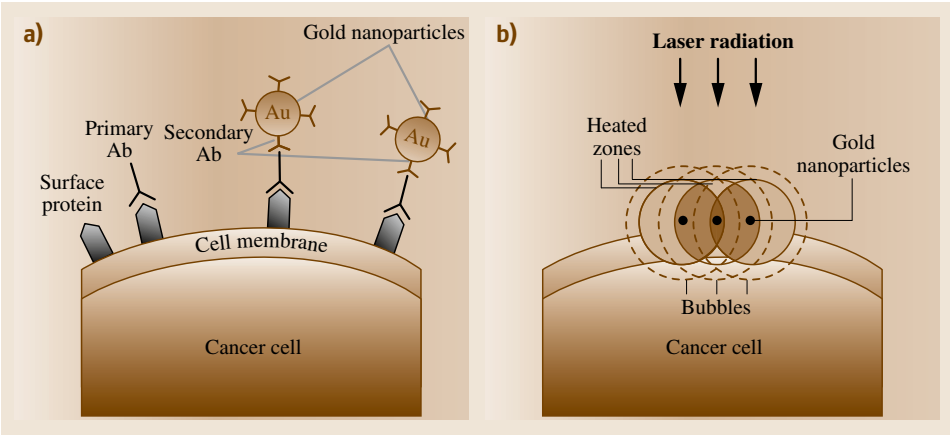

Fig. 30.1a,b Principle of selective nanophotothermolysis of cancer cell. **(a)** Cancer cell targeted with primary antibodies (Ab) which are selectively attached to secondary antibodies conjugated with gold nanoparticles. **(b)** Schematic of laser-induced heating effects around the particles

shown in Fig. 30.1a. After the nanoparticles are bound to the cancerous cells, they can be heated with electromagnetic radiation (UV/visible/IR, RF or x-ray pulses), inducing a variety of effects around the particles [30.7, 9, 11, 12], as shown in Fig. 30.1b. The heated particle can cause the cell to experience hyperthermia, resulting in surface-protein denaturing [30.13] and changing membrane permeability [30.14]. Alternatively, the nanoparticle itself can heat to the point of melting, evaporation or explosion [30.5, 6], causing further damage to cells. These effects can be used to increase the sensitivity of photoacoustic diagnosis or aid in therapy, such as selective photothermolysis, by selective thermal killing of tumor cells into which absorbing nanoparticles have been incorporated. The potential advantages of these new photothermal sensitizers heated with short laser pulses may include:

- Selective cancer-cell targeting by means of conjugation of absorbing particles (e.g., gold nanospheres, nanoshells or nanorods) with specific antibodies
- Localized tumor damage without harmful effects on surrounding healthy tissue
- Absorption at longer wavelengths in the transparency window of most biotissues
- No undesired side-effects (e.g., cytotoxicity or cutaneous photosensitivity)
- Relatively fast treatment involving potentially just one or several laser pulses.

Progress towards the development of selective nanophotothermolysis technology requires the investigation of new physical concepts and new approaches to the study of short/ultrashort laser pulse interactions with biological systems containing nanostructures. In this chapter, we develop a theory for laser-induced linear and nonlinear synergistic effects in biological cells containing nanostructures with focus on cluster aggregation, bubble formation, and nanoparticle explosion phenomena. The theory is based on our experience in theoretical studies relevant to nanoparticles [30.1, 5, 6, 12, 15–24].

30.2 Nanooptics – Lorenz–Mie Formalism

The optimal wavelength of laser radiation and optimal size range of nanoparticles for effective laser killing of cancer cells can be found by using an extended Lorenz–Mie diffraction theory, taking into account the plasmon-resonance absorption effect in metal nanoparticles. In the most general case, calculations based on the Mie theory are reduced to searching for the scattering matrix of j particles, $S^j(\theta, \phi)$, consisting of four complex functions, $S_i^j\ (\theta, \phi)$ $(i = 1, \ldots, 4)$, describing the amplitude and phase of a scattered scalar wave in any direction. Forward scattering $(\theta = 0°)$ contains the attenuation process of an electromagnetic wave, and for the case of spherical particles, $S_3^j = S_4^j = 0$. We can limit the description to a single scattering amplitude function

$$S^j(0) = S_1^j(0) = S_2^j(0) = \frac{1}{2}\sum_{l=1}^{\infty}(2l+1)\left(a_l^j + b_l^j\right) . \tag{30.1}$$

The Mie coefficients a_l and b_l contain the characteristics of the dispersal medium and are calculated through the cylindrical Bessel function of the first kind $\psi_l(y)$ and the Hankel function of the second kind $\xi_l(\rho)$, both with half-integral indices

$$a_l = \frac{\psi_l'(y)\psi_l(\rho) - \tilde{m}\psi_l(y)\psi_l'(\rho)}{\psi_l'(y)\xi_l(\rho) - \tilde{m}\psi_l(y)\xi_l'(\rho)} ,$$
$$b_l = \frac{\tilde{m}\psi_l'(y)\psi_l(\rho) - \psi_l(y)\psi_l'(\rho)}{\tilde{m}\psi_l'(y)\xi_l(\rho) - \psi_l(y)\xi_l'(\rho)} . \qquad (30.2)$$

Here, $\tilde{m} = m_0/m_1$ is the relative value of the refractive index of the medium; $m_0 = n_0 - \mathrm{i}\chi_0$ and $m_1 = n_1 - \mathrm{i}\chi_1$ are the complex refractive indices of the particle material and the aqueous suspension, respectively; $\rho = 2\pi r_0/\lambda$ is the Mie parameter; and $y = 2\pi r_0 n_0/\lambda$, $\psi_l(u) = (\pi u/2)^{1/2} J^{(1)}_{l+1/2}$, $\xi_l(u) = (\pi u/2)^{1/2} H^{(2)}_{l+1/2}$, and $\psi_l' = \mathrm{d}\psi_l(u)/\mathrm{d}u$. With knowledge of $S^j(0)$, it is possible to calculate the integrated optical performance of the particles (i. e., the dimensionless efficiency coefficients of scattering, $K^j_{\mathrm{sca}}(\rho,\tilde{m}) = \sigma^j_{\mathrm{sca}}(\rho,\tilde{m})/\sigma_0$, absorption, $K^j_{\mathrm{abs}}(\rho,\tilde{m}) = \sigma^j_{\mathrm{abs}}(\rho,\tilde{m})/\sigma_0$, and attenuation, $K^j_{\mathrm{att}}(\rho,\tilde{m}) = \sigma^j_{\mathrm{att}}(\rho,\tilde{m})/\sigma_0$, of the radiation at a given wavelength) as

$$K^j_{\mathrm{att}}(\rho,\tilde{m}) = \frac{4\pi}{k^2}\,\mathrm{Re}\left[S^j(0)\right] ,$$
$$K^j_{\mathrm{sca}}(\rho,\tilde{m}) = \frac{2}{\rho^2}\sum_{l=1}^{\infty}(2l+1)\left\{\left|a_l^j\right|^2 + \left|b_l^j\right|^2\right\} ,$$
$$K^j_{\mathrm{abs}}(\rho,\tilde{m}) = K_{\mathrm{ext}}(\rho,\tilde{m}) - K_{\mathrm{sca}}(\rho,\tilde{m}) , \qquad (30.3)$$

where $k = 2\pi/\lambda$ is the wavenumber, and $\sigma^j_{\mathrm{sca}}(\rho,\tilde{m})$, $\sigma^j_{\mathrm{abs}}(\rho,\tilde{m})$, $\sigma^j_{\mathrm{att}}(\rho,\tilde{m})$, and σ_0 are the scattering, absorption, attenuation, and geometric cross-sections of j particles, respectively.

In a simulation of electromagnetic wave propagation in a dispersed medium, our previously developed effective algorithm [30.25] was used. Here, the cylindrical functions of real or imaginary arguments and their derivatives, which occur in the expressions for the Mie coefficients a_l and b_l (30.2), are calculated as the ratio of the function and its derivative by using the recurrence relationships for direct and inverse recursions. Such an approach allows us to make an effective and accurate determination of the optical properties of a dispersal medium over a broad range of Mie parameters, $\rho = 2\pi r_0/\lambda = 0.001-1500$, below the diffraction limit simultaneously with small and large values of the real n_0 and the imaginary χ_0 parts of the refractive index of the particle's and surrounding medium substance.

30.3 Optical Properties of Gold Nanoparticles in Biological Media

The Lorenz–Mie formalism (30.1–30.3) requires the use of two dimensionless input parameters, $\rho = 2\pi r_0/\lambda$ and $\delta = \rho\tilde{m}$, where $\tilde{m}$ is the relative value of the complex refractive index of the nanoparticles in the surrounding medium at the wavelength λ. We examine the effects of the medium refractive index on the light-absorbing properties of gold particles in suspension as well as attached to a surface. Four media are used, namely water, cytoplasm, cell membrane, and collagen. The refractive indices of the media at the different wavelengths and the results of the Mie theory calculations of the maximum light-absorption factor (K_{abs}), wavelength ($\lambda_{\max}$), and radius ($r_{\max}$) for gold particles in media of different refractive indices are listed in Table 30.1. Results of computer simulations of the absorption coefficient K_{abs} as a function of the wavelength and radius of gold nanoparticles in various biological media are plotted in Fig. 30.2. Figure 30.2a shows the absorption spectrum of the gold particle over the visible range $\lambda = 400-700$ nm, and Fig. 30.2b illustrates the dependences of K_{abs} on particle size for different surrounding biomedia.

As follows from calculations, the optical properties of the gold nanosphere in low-absorbing biological media are substantially different from the case of the surrounding water medium. The maximal peak of the absorption factor increases continuously with increase in the refractive index of the surrounding media, and the color of the incident light changes from green to red; i. e., there is a red-shift effect of the absorption maximum with refractive index (Fig. 30.2a). Maximum absorption by gold nanoparticles is observed for the surrounding collagen medium, where the absorption cross-section of the gold nanoparticle exceeds its geometric cross-section by a factor of 5 for the optimal wavelength 549 nm. The presence of the low-absorbing biological surroundings also shifts the optimal radius of the gold nanoparticle for effective absorption to a smaller size region from 35 nm for the water medium to 26 nm for the collagen case (Table 30.1).

Table 30.1 Mie theory optima for the absorption factor (K_{abs}), wavelength (λ_{max}), and radius (r_{max}) for gold particles in biomedia of different refractive indices used in the simulations

Surrounding medium	λ (nm)	Refractive index n_1	K_{abs} (max)	λ_{max} (nm)	r_{max} (nm)	Surrounding medium	λ (nm)	Refractive index n_1	K_{abs} (max)	λ_{max} (nm)	r_{max} (nm)
Cytoplasm	400	1.35	4.145	540	33	Cell membrane	400	1.54	4.743	547	28
	500	1.36					500	1.5			
	600	1.365					600	1.46			
	700	1.367					700	1.4			
Blood	400	1.354	4.376	542	30	Collagen	400	1.6	4.954	549	26
	500	1.4					500	1.55			
	600	1.39					600	1.5			
	700	1.383					700	1.45			

Table 30.2 Example of absorption efficiency values for different nanoparticle shapes and structures at various wavelengths

Nanoparticle type	Effective radius (nm)	Wavelength (nm)	Absorption efficiency	References
Gold	35	532	3.50	
nanospheres	40	550	4.02	
Silica–gold	120	1100	3.5	[30.26]
nanoshells	120	750	3.75	
Gold nanorods	11.4	800	14.0	[30.26]
	17.9	825	14.5	

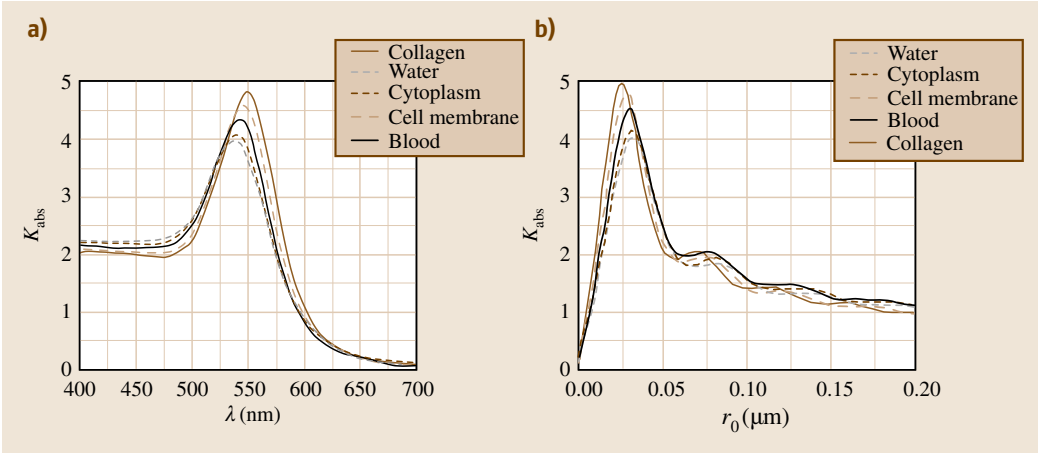

Fig. 30.2 **(a)** Absorption spectrum of the gold nanoparticle over the visible range $\lambda = 400–700$ nm. **(b)** Absorption efficiency K_{abs}, as a function of particle size for different surrounding biomedia

Thus, the absorption efficiency of gold nanoparticles is considerably higher in the low-absorbing biological media in comparison with the surrounding water medium.

The optical properties of the nanoparticles depend on the shape and internal structure of the particle as well. Table 30.2 contains results of calculations for the absorption efficiency of gold nanospheres, silica–gold nanoshells, and gold nanorods. For gold nanoparticles, the highest absorption efficiency is observed for nanorods; however, silica–gold nanoshells are tunable over the longer wavelengths in the transparency window of most biotissues. We should note that other materials can exhibit strong absorption efficiency, e.g., silver nanospheres, which show strong absorption around 394 nm in the UV range of spectrum.

30.4 Kinetics of Heating and Cooling of Nanoparticles

30.4.1 Time Dynamics of the Nanoparticle Temperature

In this section, we use the heat transfer equation with several simplifying assumptions to calculate the nanoparticle temperature as a function of time. It has been shown by *Letfullin* et al. [30.20] that a one-temperature model (OTM) is appropriate for plasmonic nanoparticle heating for lasers of pulse durations in the femto-, pico-, and nanosecond ranges. The first approximation used in this model is that the electron and lattice temperatures are equal (due to fast transfer of electron heat to the phonon subsystem). This provides the following heat–mass transfer rate equation for a single lattice temperature $T_s(t, r)$ that describes the laser interaction with the particle and surrounding medium

$$\frac{\mathrm{d}}{\mathrm{d}t}T_s(t,r) = \frac{\mu_s(T_s)}{\rho_s C_s(T_s)}\Delta T_s(t,r) + \frac{Q(t,r)}{\rho_s C_s(T_s)} - j_D(T_s)S_0 + \frac{3L}{r_0 C_s(T_s)}\frac{\mathrm{d}r_0}{\mathrm{d}t}\,. \tag{30.4}$$

Here, $\Delta = \partial^2/\partial x^2 + \partial^2/\partial y^2 + \partial^2/\partial z^2$ is the Laplace operator; $\mu_s(T_s)$, $C(T_s)$, L, ρ_s, and r_0 are, respectively, the heat conductivity of the surrounding medium and the specific heat, evaporation heat, density, and radius of the nanoparticle. The second assumption is that the particle is heated uniformly across the volume of the particle, i. e., $\Delta T_s(t, r) = 0$, provided that each point inside the particle volume has the same temperature $T_s(t)$. This homogeneous heating approximation can be applied if the heat diffusion time τ_D is less than the duration of the laser pulse: $\tau_D = r_0^2/4\chi < \tau_L$, where r_0 is a particle radius, χ is the thermal diffusivity of the particle material, and τ_L is the laser pulse duration. For gold nanoparticles with $r_0 = 20\,\mathrm{nm}$ and $\chi = 1.18\times10^{-4}\,\mathrm{m^2/s}$, τ_D is about $10^{-12}\,\mathrm{s}$. This is appropriate for heating of metal nanoparticles by pico- and nanosecond laser pulses and allows the use of a simplified relationship for the power density of the energy generated $Q(t, r_0)$ in the particle

$$Q(t, r_0) = \frac{3K_{abs}(r_0, \lambda)I_0 f(t)}{4r_0}\,. \tag{30.5}$$

Here, $K_{abs}(r_0, \lambda)$ is the absorption efficiency of the nanoparticle, $f(t)$ is the time profile of the laser pulse, and I_0 is the incident intensity of the laser pulse. The experiments analyzed utilize Gaussian beam profiles in the form $f(t) = \mathrm{e}^{-(at-b)^2}$; the coefficients are adjusted to create a pulse profile with the pulse duration of the laser used in the experiments. Another approximation limits heat loss to diffusion from the particle surface into the surrounding medium, defining the energy flux density $j_D(T_s)$ as

$$j_D(T_s) = \frac{\mu_\infty T_s}{(\alpha+1)r_0^2 C_s(T_s)\rho_s}\left[\left(\frac{T_s}{T_\infty}\right)^{\alpha+1} - 1\right], \tag{30.6}$$

where μ_∞ and T_∞ are, respectively, the heat conductivity and temperature of the surrounding medium at equilibrium; α is an exponent set to make the dynamics between the particle and medium more realistic; $\alpha > 1$ relates to high thermophysical characteristics of the surrounding medium, while $\alpha < 1$ relates to low thermophysical characteristics such as insulators; $\alpha = 1$ is a good approximation for biological media, which are of interest in the present chapter. The last assumption is that the particle temperature remains below the temperature of evaporation, which sets the last term in (30.4) to zero. The result (30.7) determines the particle temperature in terms of the energy accumulation from the incident laser radiation in the first term and energy loss due to heat diffusion into the medium in the second term

$$\frac{\mathrm{d}}{\mathrm{d}t}T_s = \frac{3K_{abs}(r_0, \lambda)I_0 f(t)}{4r_0\rho_s C_s(T_s)} - \frac{\mu_\infty T_s}{(\alpha+1)r_0^2 C_s(T_s)\rho_s}\left[\left(\frac{T_s}{T_\infty}\right)^{\alpha+1} - 1\right]. \tag{30.7}$$

30.4.2 Comparison of Single-Pulse and Multipulse Modes of Heating

The extent of the particle heating by radiation depends on many factors, divided primarily into three categories: (1) particle material, size, and shape; (2) laser pulse wavelength, energy density, duration, pulse shape, and generation frequency; and (3) properties of the surrounding medium. Even with the many factors involved in an experimental setup that contribute to the individual heating characteristics of a nanoparticle, several factors stay relatively constant across many experimental situations. Specifically, spherical gold nanoparticles are commonly used because they are relatively easy to fabricate, nontoxic, easily conjugated to antibodies, and strong absorbers [30.27]. Nanosecond pulse-width lasers with pulse firing frequencies of 10 Hz are often used because they are widely available and cheaper than pico- and femtosecond lasers or lasers with higher firing

Table 30.3 Experimental data for multipulse laser nanoparticle heating

Reference	[30.7]	[30.9]	[30.12]	[30.28]	[30.29]	[30.30]	[30.31]
Laser	**Nd:YAG**	**Nd:YAG**	**Nd:YAG**	**Nd:YAG**	**Nd:YAG**	**Ti:sapphire**	**Nd:YAG**
Wavelength (nm)	532	565	532	532	532	750	1064
Pulse energy (J/cm^2)	0.5	0.5	0.5	0.13	0.03	0.95	0.002
Pulse duration (ns)	12	20	12	6	7	10	7
Frequency of generation (Hz)	10[1]	10[1]	10[1]	10	20	11.8 MHz/ 50 MHz	10
Particle							
Material	Gold	Gold	Gold	Gold	Iron oxide	Gold	Gold
Structure	Sphere	Sphere	Sphere	Sphere	Sphere	Rod	Rod
Diameter (nm)	40	30	40	21/4.9	10	23.6[2]	22.76[2]
Aspect ratio	–	–	–	–	–	3.2	5.9
Other							
Number of pulses	100	100	30	3000	600	2	10
Surrounding medium	PBS	PBS	Water	Water	Water	Water	Water

[1] HOYA ConBio MedLite C Series and IV Series Nd:YAG lasers have a maximum generating frequency of 10 Hz, so the generation frequency for lasers when not provided was assumed as 10 Hz.
[2] It is common to use an effective radius (r_{eff}) when the particle is of nonstandard shape; this is the radius of a sphere that provides the equivalent volume as an arbitrary shape.

frequencies. Additionally, water or phosphate-buffered saline (PBS) solution is used as a surrounding medium due to strong similarities with a biological cell. Several experiments that use these factors are studied in our analysis [30.7, 8, 12, 28–31].

In experiments, *Zharov* et al. [30.7] used nanoparticle heating for bacterial killing. Spherical gold nanoparticles of diameter 10, 20, and 40 nm were heated with laser light, and it was determined that, at 3–5 J/cm^2, only 1–3 pulses are required for harmful effects on bacteria, while at 0.5–1 J/cm^2, at least 100 pulses are required to produce harmful effects. *Pitsillides* et al. [30.9] explored micro- and nanoparticles for selective cell therapy, finding that, for 20 nm-diameter gold nanospheres irradiated by 20 ns, 532 nm pulses at 0.5 J/cm^2, there is a much greater correlation of the number of particles attached to the cell than of the number of pulses when considering cellular damage. *Zharov* et al. [30.12] investigated bubble formation from nanoparticles. Using a smooth distribution of 40 nm-diameter gold nanospheres on a cell, they found that that 30 pulses of 0.5 J/cm^2 or one pulse of ≈ 2 J/cm^2 results in complete cell death. Alternatively, with cluster formation, cell damage occurs after 100 laser pulses at 80 mJ/cm^2. *Peng* et al. [30.28] focused on the effects of laser irradiation on particle size and peak absorption wavelength. They showed, using a Nd:YAG laser and 21 nm spherical gold nanoparticles, that irradiation causes the particles to fragment to an average diameter of 4.9 nm, changing the peak absorption wavelengths. *Kalambur* et al. [30.29] used iron oxide nanoparticles to compare RF heating with multipulse laser heating and determined that multipulse lasers produce a higher cellular uptake of particles, enabling greater cellular damage. *Hleb* and *Lapotko* [30.30] used gold nanorods to determine high-energy effects of lasers on nanorods and nanospheres, such as how long the particles maintain photothermal properties (before deterioration) and the effects of multiple pulses in the form of a *pulse train*, determining that very rapid pulse repetition leads to increased bubble effects. Lastly, *Takahashi* et al. [30.31] used gold nanorods irradiated with multipulse near-IR lasers to find that selective cell damage is achievable.

One of the greatest potential benefits from multipulse lasers is accumulative heating in the target. If multipulse lasers could be used to quickly accumulate heat in nanoparticles with many consecutive low-energy pulses, then the laser energy density would not be a prohibitive aspect of the treatment. Multiple low-energy-density pulses could be used rather than a single high-energy-density pulse to achieve the same nanoparticle temperature, sparing healthy cells from excessive heating as well as ensuring that the energy density required for treatment is below the medical standard of 100 mJ/cm^2 [30.12].

The focus of this section is to compare and contrast the effects of multipulse (set of short pulses) versus single-pulse laser heating of nanoparticles. The laser

Table 30.4 Additional input parameters for the theoretical calculations

Reference	[30.7]	[30.9]	[30.12]	[30.28]	[30.29]	[30.30]	[30.31]
Particle							
Calculated absorption efficiency	2.7225[1] ($\lambda = 532$ nm)	0.72[1] ($\lambda = 565$ nm)	2.72250 ($\lambda = 532$ nm)	1.29367 ($\lambda = 532$ nm)	1.68663 ($\lambda = 532$ nm)	11.5[2] ($\lambda = 725$ nm)	15.75[2] ($\lambda = 860$ nm)
Specific heat (J/(kg K))	129	129	129	129	937	129	129
Density (kg/cm^3)	0.0193	0.019	0.0193	0.0193	0.00524	0.0193	0.0193
Initial temperature (K)	300	300	300	300	300	300	300
Laser							
Energy density (J/cm^2) (original/revised)	0.5/0.01	0.5/0.1	0.5/0.01	0.13/0.0325	0.03	0.95/0.01	0.002
Medium							
Thermal conductivity (W/(cm K))	0.0075	0.0075	0.0060	0.0060	0.0060	0.0060	0.00604

[1] Absorption efficiency values calculated for nanoparticles in water due to difficulty in obtaining refractive index data for PBS solution
[2] Estimated absorption efficiency from *Jain* et al. [30.26] based on the effective radius and aspect ratio of the nanorods, using the closest values given based on wavelength r_{eff} and aspect ratio

heating of nanoparticles is very sensitive to the time structure of the incident pulsed laser radiation, i.e., the pulse shape and duration, and the number of pulses per unit time. We limit the maximum temperature of the theoretical calculations to the melting point of the material ($T_M \approx 1336$ K for bulk gold material and remaining above 1100 K for gold particles larger than 5 nm in diameter [30.32]) so that the particles will not undergo advanced phenomena of heating (evaporation, melting or explosion), but require that the nanoparticles surpass 433 K as required for protein denaturing [30.27].

The summary data obtained from experimental papers [30.7, 8, 12, 28–31] can be found in Table 30.3, while the additional input data we use for our calculations are listed in Table 30.4. We modified the energy density when the particle temperature exceeds the melting point of the material to reduce the particle temperature into our range of interest.

Peng et al. [30.28] used an incident energy density (0.13 J/cm^2) at a wavelength of 532 nm that causes particles to exceed the melting point, resulting in fragmentation. To make a case for reducing the incident energy density, we performed calculations to determine how changing the energy density would change the time–temperature profile of the nanoparticle heating and cooling. Our calculations show that changing the energy density has no effect on the time it takes for the particle to heat to the maximum temperature. Figure 30.3 demonstrates this with three different time–temperature profiles for: a 21 nm-diameter gold sphere irradiated by a 0.13 J/cm^2 pulse (solid line) and 0.0325 J/cm^2 pulse (dashed line), and a 4.9 nm-diameter gold sphere irradiated by a 0.13 J/cm^2 pulse (dotted line). Changing the energy density from a 0.13 pulse to a 0.0325 J/cm^2 pulse has no effect on the time required for the particle

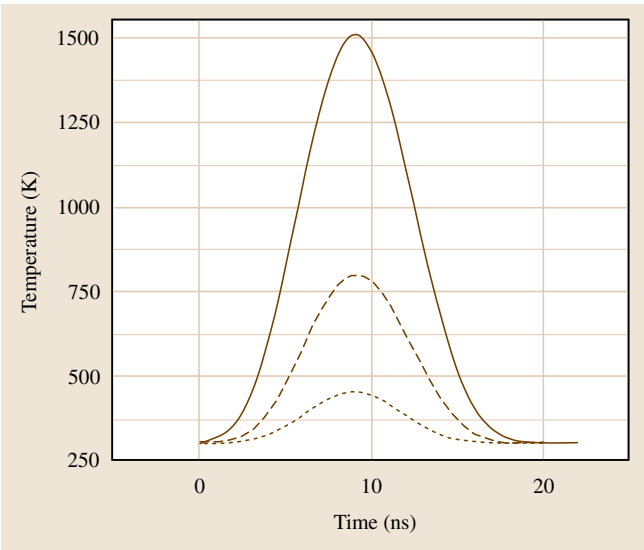

Fig. 30.3 Time–temperature profiles for 21 nm-diameter (*solid*) and 4.9 nm-diameter (*dotted*) gold particles in water irradiated by a 6 ns, 0.13 J/cm^2 pulse at 532 nm and a 21 nm-diameter gold particle irradiated by the same pulse at 0.0325 J/cm^2 (*dashed*)

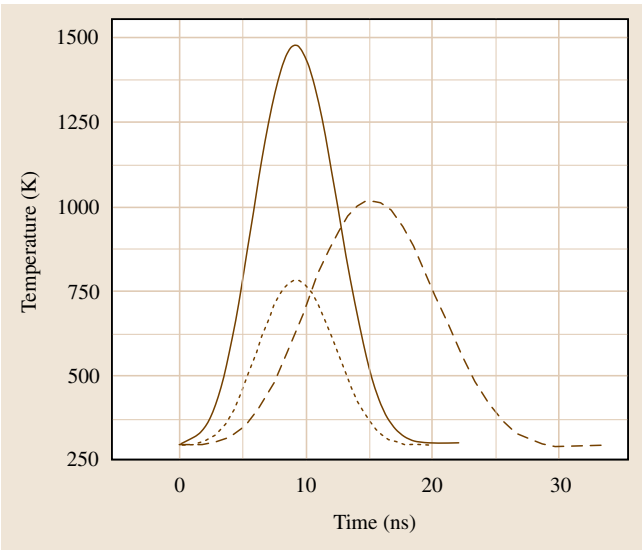

Fig. 30.4 Time–temperature profiles for 21 nm-diameter nanospheres with incident laser pulse duration of 6 ns at energy density of 0.13 J/cm^2 (*solid*) and 0.0325 J/cm^2 (*dotted*) and nanorods with effective diameter of 23.6 nm irradiated by a 10 ns, 0.01 J/cm^2 pulse (*dashed*)

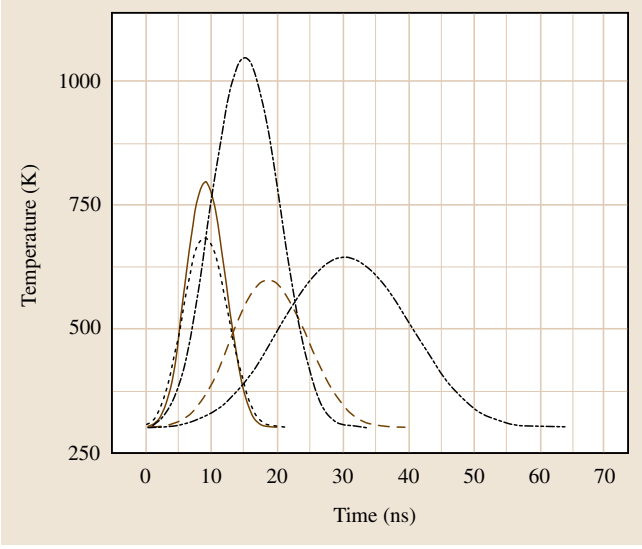

Fig. 30.5 Calculated time–temperature profiles for five different pulse durations used in single-pulse mode heating. Three gold nanosphere cases: [30.7] – 12 ns pulse (*dashed*); [30.9] – 20 ns (*dash-dot-dotted*); and [30.28] – 6 ns (*solid*). Two gold nanorod cases: [30.30] – 10 ns (*dash-dotted*); and [30.31] – 7 ns (*dotted*)

to reach its maximum temperature, which occurs 9 ns after the incident pulse in both cases.

The cooling time for the particle is slightly affected by the magnitude of the maximum temperature and is thus linked to the energy density. Heating the particles to 1500 and 800 K, respectively, for 0.13 and 0.0325 J/cm^2 pulses, we find that the cooling time is only slightly longer for the higher-energy-density pulse. For the 0.13 J/cm^2 pulse, the particle cools back to ambient temperature 11.4 ns after the peak, while for the 0.0325 J/cm^2 pulse the particle takes 10.6 ns after the maximum to cool.

Single-Pulse Mode

To analyze the effects due to varying characteristics of the experiments, in this section we compare theoretical calculations for those experiments that have contrasting characteristics, such as pulse duration, particle size and shape, and medium in the single-pulse mode of heating. Considering particle shape – between gold nanorods and gold nanospheres – we extrapolate from *Jain* et al. [30.26] that changing the particle shape significantly alters the peak absorption wavelengths and the respective coefficients of absorption, but these can be equated to spherical particles with an effective radius and aspect ratio, AR = length/diameter. In [30.30], the gold nanorods with $r_{\text{eff}} = 11.8$ nm and AR = 3.2 have an absorption efficiency around 11.5 when irradiated with 725 nm light [30.26]. Contrasted with the gold nanospheres in [30.28] ($r_0 = 11.5$ nm, $K_{\text{abs}} = 1.29$ at $\lambda = 532$ nm), a much lower energy density can be used to reach the same ablation temperature for the nanorods due to the extremely high absorption efficiency. Figure 30.4 shows the time–temperature profiles from [30.28] for nanospheres ($d = 21$ nm) under 0.13 and 0.0325 J/cm^2 pulses at 532 nm, as well as the temperature profile for the nanorods ($r_{\text{eff}} = 11.8$ nm, AR = 3.2) from [30.30] irradiated by 0.01 J/cm^2. This figure demonstrates how a much lower energy density can result in higher nanorod temperatures when compared with nanospheres of equivalent radius. The tunable characteristics of nanorods allow greater adjustment of the wavelength that will result in maximum absorption efficiency and how high the absorption efficiency will be, thus making nanorods potentially more effective for ablative treatments than nanospheres. As we will show in the next section, in terms of accumulative heating with a multipulse mode of irradiation, the difference between nanorods and nanospheres is not significant.

Another characteristic of the experimental setups [30.7, 9, 12, 28–31] is a laser pulse duration of roughly 10 ns. Figure 30.5 shows time–temperature pro-

files for five different pulse durations ranging from 6 to 20 ns. It follows from our calculations that, during the laser pulse, the transfer of heat from the nanoparticle into the surrounding media is slight, and the particle rapidly reaches its maximum temperature. The heating rate is about 10^2 K/s, depending on the pulse duration and incident energy density. The temperature of the particle continues to rise even after the end of the laser pulse. Using [30.30] as an example, the highest temperature of 1048.6 K for a 10 ns pulse is observed at a heating time of 15.2 ns, when the laser pulse has already degraded. After then, the transfer of heat from the particle to the surrounding medium becomes critical, since the energy source is no longer present in the system. The temperature of the particle and surrounding medium remains high (above 425 K) up to 24.6 ns after the pulse is fired, exceeding the laser pulse duration by 2.5 times. The total time for one cycle (heating from the initial temperature of 300 K to a maximum temperature and then cooling back to the initial temperature) is 32.8 ns, over thrice the pulse duration. Varying the pulse duration changes the maximum temperature of the particle as well as the time span of heating and cooling.

Due to the nature of the experiments and the intended application of the method for treatment of cancer inside the human body, the medium characteristics cannot be changed. Furthermore, the ability to change the material of the nanoparticle is also limited due to toxicity, but in the case of metal nanoparticles, they should all exhibit similar heating and cooling kinetics to those seen in gold and iron(III) oxide (Fe_3O_4). As we have shown above, the particle size, particle shape, and laser energy density do not significantly change the temporal behavior of nanoparticle heating and cooling, but just the magnitude of the maximum temperature reached. The laser pulse duration changes the maximum particle temperature as well as the temporal span of heating and cooling, following relatively predictable multiplicative values with respect to the pulse duration: the maximum temperature is at 1.46 times the pulse duration; the temperature remains above 425 K until 2.2 times the pulse duration; and the entire heating and cooling cycle takes about 3.23 times the pulse duration. These aspects could be useful for further single-pulse investigations, but they do not come into play when considering the multipulse heating of nanoparticles discussed below.

Multipulse Mode

Using the scaled-down energy density values determined in previous sections and a function to simulate multiple pulses, we have calculated the time profile of the nanoparticle temperature in a multipulse heating mode to determine what would enable accumulative heating of nanoparticles. To simulate multiple pulses, we use the same function as in the single-pulse simulations, but with the addition of several values of b to shift each consecutive pulse

$$f(t) = e^{-(at-b_1)^2} + e^{-(at-b_2)^2} + e^{-(at-b_3)^2} .$$

Three multipulse cases are shown in Fig. 30.6, demonstrating particle heating and cooling over time for the conditions of [30.7, 12, 29] as listed in Table 30.3. These simulations utilize a 37 and 62.5 MHz generation frequency due to the large time gap (relative to the pulse width) between each incident pulse when using the 10 Hz generation frequency specified in the references. These profiles demonstrate visually that, even at relatively high generation frequencies, multiple pulses do not produce any accumulative heating effect over time. The particle reaches the peak temperature and falls to equilibrium (300 K) in roughly three times the pulse duration, but the time delay between the pulses in experiments exceeds the pulse duration by five to ten million times.

Several of the experimental papers show effects from multipulse laser heating that are not present in the single-pulse laser mode, even though the pulse generation frequency for the multipulse mode is well below the MHz generation frequency. *Zharov* et al. [30.7] dis-

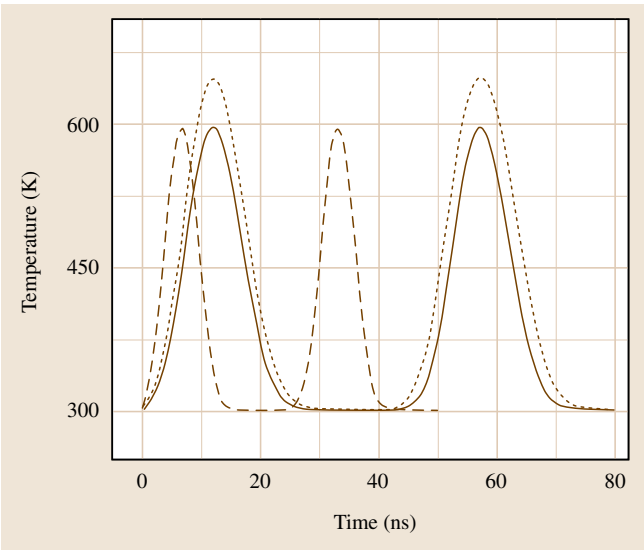

Fig. 30.6 Multipulse time–temperature profiles for [30.7] (*solid*), [30.12] (*dotted*), and [30.29] (*dashed*) with modified pulse generation frequencies

Table 30.5 Experimental data for healthy and tumor cells

Source	Cancer	Organelle	Healthy diameter (μm)	Well differentiated diameter (μm)	Moderately differentiated diameter (μm)	Poorly differentiated diameter (μm)
[30.33]	Hepatocellular carcinoma	Nucleus	7.5	8.5	8.8	10.3
[30.33]	Hepatocellular carcinoma	Mitochondria	1.1	0.9	0.9	0.66
[30.34]	Colorectal adenocarcinoma	Nucleus	5.2	7.2	–	–

Source	Cancer	Organelle	Benign diameter (μm)	In situ diameter (μm)	Invasive diameter (μm)
[30.35]	Ductal breast carcinoma	Nucleus	7	11.6	8.33
[30.36]	Intraductal breast cancer	Nucleus	8.58	–	8.97
[30.37]	Breast cancer	Nucleus	5.6	–	5.8

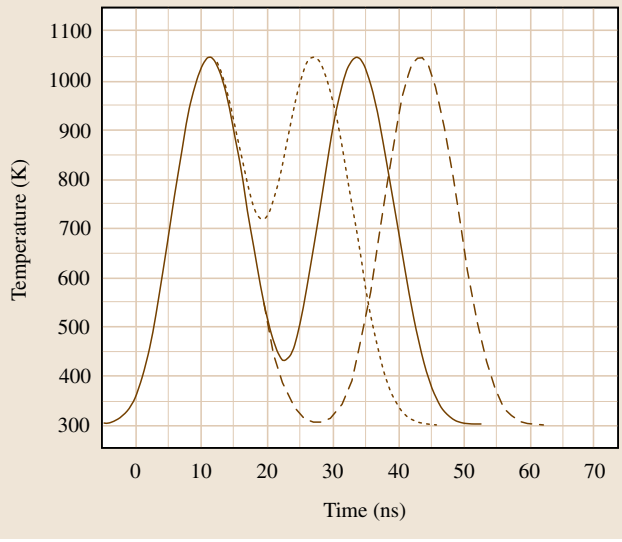

Fig. 30.7 Time–temperature profile for multipulse laser heating of gold nanorods ($r_{\text{eff}} = 11.8$ nm, AR = 3.2, $K_{\text{abs}} = 11.5$ at 725 nm) irradiated by 0.01 J/cm^2/10 ns pulses at repetition rate of 50 MHz (*dashed*), 66.6 MHz (*solid*), and 80 MHz (*dotted*)

cussed bacterial killing and find that, at 3–5 J/cm^2, only 1–3 pulses are required for bacterial damage, while at 0.5–1 J/cm^2 more than 100 pulses are required. We feel the reason for these effects are that at 3–5 J/cm^2 the particles undergo phenomena beyond simple heating and ablation of the surrounding cell due to the extremely high temperature of the nanoparticle, and thus have a large area of effect. In the case of 0.5–1 J/cm^2 pulses, the nanoparticles can still surpass the melting threshold, but without extreme particle phenomena (such as explosion) being observed. In either case, each pulse is incident on ambient-temperature particles, raising their temperature to the critical temperature for cell death. Additionally, the energy densities involved are well above the medical standard of 100 mJ/cm^2, so such results are helpful to show the high-energy phenomena and potential treatment options. However, the methods of implementing treatment require refinement before direct medical applications can be developed. Our current investigation to determine the potential of accumulative heating effects in metal nanoparticles is an attempt at localizing damage to cancer cells by using low-energy density lasers while still killing the cancer cells.

After determining that most other experimental characteristics (such as pulse duration, particle size, etc.) have no ability to create an accumulative heating phenomenon of interest in metal nanoparticles, the pulse generation frequency used in multipulse scenarios was tested with a high-pulse generation frequency experiment by *Hleb* and *Lapotko* [30.30]. This experiment uses two pulses of 10 ns duration that are separated by 20 and 150 ns time intervals (50 and 6.67 MHz, respectively). Figure 30.7 shows three different multipulse calculations based on the experimental setup used in [30.30] for gold nanorods ($r_{\text{eff}} = 11.8$ nm,

Table 30.6 Computational input data for OTM calculations

Source	Cancer	Organelle	Organelle state	Diameter (μm)	Absorption efficiency (at λ = 700 nm)[1]
[30.33]	Hepatocellular carcinoma	Nucleus	Healthy	7.5	0.944183362
			Well differentiated	8.5	0.964865712
			Moderately differentiated	8.8	0.969903343
			Poorly differentiated	10.3	0.989209877
[30.33]	Hepatocellular carcinoma	Mitochondria	Healthy	1.1	0.134234082
			Well differentiated	0.9	0.110949860
			Moderately differentiated	0.9	0.110949860
			Poorly differentiated	0.66	0.082130836
[30.35]	Ductal breast carcinoma	Nucleus	Benign	7.0	0.930908259
			In situ	11.6	1.000194442
			Invasive	8.33	0.961677234
[30.36]	Intraductal breast cancer	Nucleus	Benign	8.58	0.966255375
			Invasive	8.97	0.972557278
[30.37]	Breast cancer	Nucleus	Benign	5.6	0.880181004
			Invasive	5.8	0.889019082

[1] 700 nm was chosen because it is the wavelength with the greatest absorption efficiency difference between cancerous and healthy organelles at a wavelength in the range of 400–1000 nm

Table 30.7 Organelle and cytoplasm properties

Organelle	Diameter d (μm)	Specific heat c (J/(kg K))	Thermal conductivity μ (W/(m K))	Density ρ (kg/m^3)
Nucleus	5 [30.38], 5–10 [30.39], 7.5–10 [30.40], 5–10 [30.42]	3000 [30.41]	0.3 [30.41]	1050 [30.41], 1400 [30.42]
Mitochondria	0.85–1.15 [30.38], 1–3.57 [30.39], 0.87–3.57 [30.40], 1–2 [30.42]	3000 [30.41]	0.3 [30.41]	1050 [30.41], 1100 [30.42]
Ribosome	0.025 [30.4], 0.025 [30.40], 0.02 [30.42]	3000 [30.41]	0.3 [30.41]	1050 [30.41], 1600 [30.42]
Microtubules	0.025 [30.38], 0.028 [30.39], 0.02 [30.40], 1–2 [30.42]	3000 [30.41]	0.3 [30.41]	1050 [30.41], 1100 [30.42]
Cytoplasm	–	4180 [30.41]	0.59 [30.41]	

AR = 3.2, $K_{abs} = 11.5$ at 725 nm) in water irradiated by 0.01 J/cm^2 using 10 ns pulses with generation frequency of 50, 66.6, and 80 MHz. We exclude the case with pulse separation of 150 ns due to the previously shown rapid cooling of metal nanoparticles (32.8 ns for a 10 ns pulse in [30.30]) as well as the experimental result by *Hleb* and *Lapotko* [30.30] that there are no additional effects from two pulses separated by 150 ns over a single pulse. Even at the high pulse generation frequencies shown, the 10 ns pulse does not create an accumulative heating effect in the metal nanoparticles. Furthermore, changing the pulse duration concurrently with high-frequency pulse generation simulations only changes the magnitude of the maximum particle temperature but does not enable the accumulative heating effect in the metal nanoparticles of interest to our investigation.

Multipulse Heating of Healthy and Cancerous Cell Organelles

Using the multipulse form described above, we also tested the heating and cooling kinetics of biological cell organelles to determine the ability to selectively destroy cancer cells. Acquiring data for organelles (nucleus, mitochondrion, and ribosome) is difficult due to the wide variety of situations under which they must act; the added complexity of the large number of cancers makes finding very specific data difficult. Using a variety of

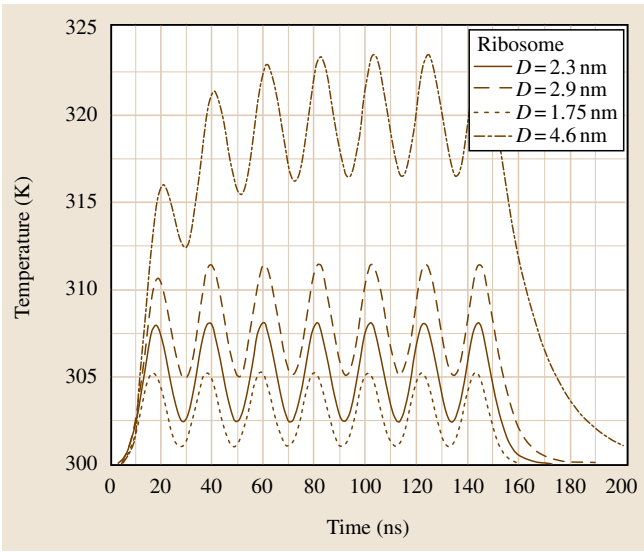

Fig. 30.8 Ribosomal time–temperature profiles at various diameter values. Multipulse laser parameters: 12 ns duration, 0.1 J/cm^2 at $\lambda = 700$ nm; $b_1 = 2.5$, $b_2 = 6$, $b_3 = 9.5$, $b_4 = 13$, $b_5 = 16.5$, $b_6 = 20$, and $b_7 = 23.5$

cited dimensions and organelle properties (Tables 30.5–30.7), we have calculated the *average* organelle size to determine the theoretical effects of the multipulse mode of laser irradiation on the organelle temperature with the same procedure as detailed above.

The cell organelles demonstrate the heat accumulation effect due to the multipulse mode of heating as shown in Figs. 30.8 and 30.9. The ribosomal heating in Fig. 30.8 contrasts with heating for the nuclei and mitochondria in Fig. 30.9; the ribosomes do not experience accumulative heating to the extent that nuclei or mitochondria do, based primarily on the much smaller size. Even with the small size, within the first few pulses the accumulative heating effect is apparent, which contrasts with any nanoparticle simulations previously discussed. The much higher values of specific heat in the organelles and the thermal conductivity of the medium is what causes the organelles to undergo accumulative heating, whereas metal nanoparticles do not experience accumulative heating, even at high-frequency pulse generation rates. This gives an advantage for organelles in using the multipulse versus single-pulse mode, since

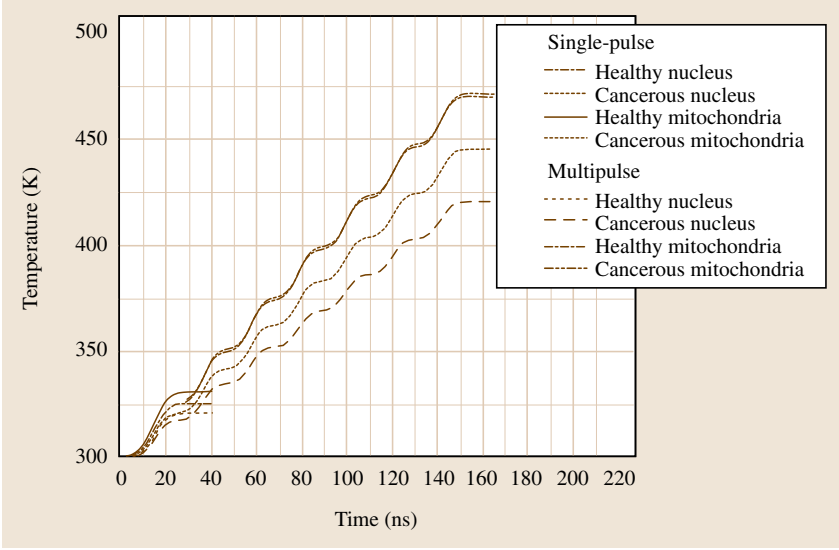

Fig. 30.9 Both single- and multipulse laser heating for *average* organelles. Average values: healthy nucleus (7.17 μm), cancerous nucleus (8.97 μm), healthy mitochondria (1.1 μm), and cancerous mitochondria (0.82 μm). Single-pulse laser parameters include a 0.1 J/cm^2 pulse at 700 nm wavelength

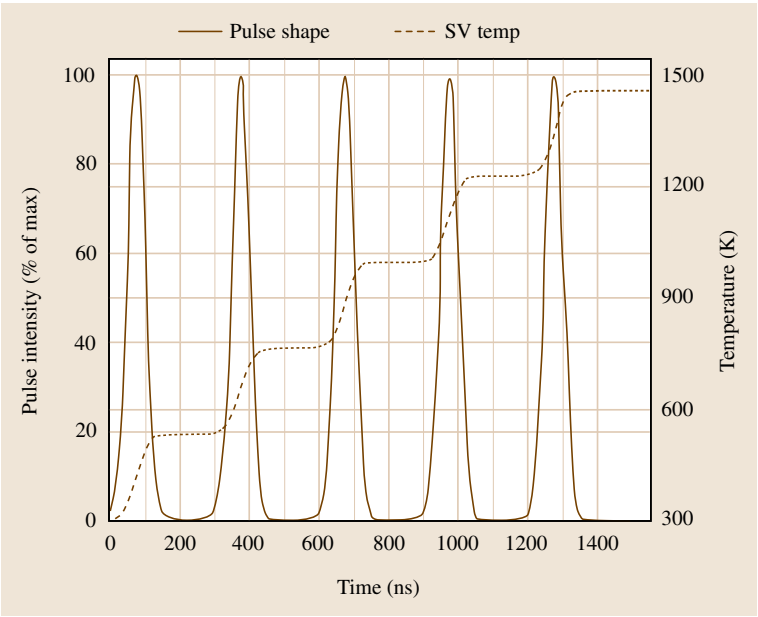

Fig. 30.10 Multipulse mode of heating of bone tissue. A representative multipulse function is drawn with a *solid line*, and the heating kinetics with a *dashed line*, showing five 30 mJ pulses of 60 ns pulse width repeating every 300 ns

the laser energy density per pulse can be reduced dramatically below the safety standard for medical usage of lasers. In this case, any desired final temperature of the organelle can be reached easily by adjusting the number of pulses at low-energy density per pulse.

While the organelles demonstrate a similarity in the heat accumulation effect, both the mitochondria and nuclei respond differently to the pulsed mode of heating. As shown in Fig. 30.9, healthy and cancerous mitochondria do not respond differently in a significant way to laser heating, while the healthy nucleus is heated 40 K higher than the cancerous nucleus. The difference in heating characteristics is due to several behavioral properties: the size of the nucleus is much larger than mitochondrion, mitochondrion has been shown to shrink when in cancerous cells, and the nucleus of cancerous cells is known to grow relative to their healthy cell size. The dynamics of size on temperature results in the mitochondria being heated to a higher temperature, but with very little specificity. Alternatively, nuclei are heated to a lower temperature at a higher specificity level, though the healthy nuclei are the first to get damaged. The potential method of selectively heating cancerous organelles to kill cancer cells is shown to be ineffective with our calculations due to the higher heating temperatures of mitochondria and the lower heating of cancerous nuclei. With that in mind, the effects of accumulative heating are very apparent.

The results of the simulation using cell organelles demonstrate the slow rate of the cooling kinetics of the biological particles. This allows for accumulation of heat by a multipulse heating mode for hard tissue, such as bone and teeth as well, as shown in [30.22, 23]. Here, the bone hydroxyapatite particles were heated by single- and multipulse laser pulses of 2.12 μm wavelength. Figure 30.10 shows the results for bone tissue temperature increase by five 0.03 J pulses. To reach the same maximum temperature in the bone tissue ($T_{max} = 1460$ K) using a single pulse requires a much higher energy per pulse of about 0.15 J. Thus, the multipulse mode could be utilized to attain the higher temperatures required for tissue ablation using many pulses with low individual energies. This gives a large amount of control over the individual pulse energies, which is especially important in medical and dental laser applications where regulations may limit the maximum pulse energies for different procedures.

Summary of the Heating Kinetics

We have performed time-dependent simulations and detailed analyses of different nonstationary laser–nanoparticle interaction modes to determine the accumulative heating potential of metal nanoparticles irradiated by multipulse lasers. Our analysis of the single-pulse mode of heating of metal nanoparticles in a biological cell environment has shown that alterations to the particle size, shape, and material (metal) all have

effects on the magnitude of the maximum particle temperature. Additionally, modifications to the laser energy density or wavelength can be used to change the maximum particle temperature. The most substantial change within single-pulse heating is the effect of pulse duration on the time dynamics of particle heating and cooling. By increasing the pulse duration, the maximum nanoparticle temperature decreases, but heating and cooling both take longer and allow for a longer time period when the nanoparticles are above the denaturing temperature of 433 K. This increased duration of high particle temperature could prove beneficial to ensure cellular damage. Alternatively, decreasing the pulse duration increases the maximum temperature reached by the nanoparticles while decreasing the time for heating and cooling. Such laser parameter modifications could allow for easier and more refined treatment than modification of particle size or shape, while still having dramatic implications for the effectiveness of the treatment.

Our simulations have shown that, at the instant when the laser pulse stops, the cooling rate reaches almost the same values as a heating rate due to the large surface area of the nanoparticle and high thermal conductivity of the surrounding aqueous medium. This becomes crucial for the multipulse mode of heating the metal nanoparticles. From our analysis of multipulse metal nanoparticle heating, we have determined that the multipulse mode of heating does not create accumulative heating effects in metal nanospheres or nanorods (diameters of 5–40 nm) due to the rapid cooling kinetics of metal nanoparticles in an aqueous environment.

However, changing the target material to biological particles, such as cell organelles or hard tissue particles with much higher values of specific heat, causes the biological particles to undergo accumulative heating, whereas metal nanoparticles do not experience accumulative heating, even at high frequency generation rates. The accumulative heating effect provides an advantage for organelles and biological tissue in using the multipulse versus single-pulse mode, since the laser energy density per pulse can be reduced dramatically below the safety standard for medical usage of lasers. In this case, any desired final temperature of the biotissue can be reached easily by adjusting the number of pulses at low energy density per pulse.

30.5 Spatial Distribution of Temperature Fields Around the Nanoparticle

30.5.1 Theoretical Model

For simulations of the spatial distribution of temperature in and outside the nanoparticle, we solve the heat–mass transfer equation (30.4) in a quasistationary heating approximation, namely $\mathrm{d}T_\mathrm{s}(r,t)/\mathrm{d}t = 0$. In this approximation, we neglect the time required to reach the maximum temperature (extremum of the $T_\mathrm{s}(t)$ curve) of the nanoparticle and solve the heat diffusion equation for the spatial distribution for that particular temperature. We use here the heat transfer model developed by *Goldenberg* and *Tranter* [30.43] for a uniformly heated, homogeneous sphere embedded in an infinite homogeneous medium. Consider a homogeneous sphere of radius r_0 surrounded by an infinite homogeneous medium, with heat produced in the sphere for time $t > 0$ at the constant rate A per unit time per unit volume. Since the surrounding medium is transparent to the chosen wavelength, we can neglect thermally induced changes in the cellular refractive index during the action of a nanosecond laser pulse. Both the sphere and medium are initially at zero temperature. Let the subscript "1" refer to the sphere and "2" to the medium, and T, μ, and χ denote the temperature, thermal conductivity, and diffusivity, respectively. Then, the heat transfer equations with boundary conditions are

$$\left.\begin{aligned} \frac{1}{\chi_1}\frac{\partial T_1}{\partial t} &= \frac{1}{r^2}\frac{\partial}{\partial r}\left(r^2\frac{\partial T_1}{\partial r}\right) + \frac{A}{\mu_1}\,, \\ &\quad 0 \le r < r_0\,, \\ \frac{1}{\chi_2}\frac{\partial T_2}{\partial t} &= \frac{1}{r^2}\frac{\partial}{\partial r}\left(r^2\frac{\partial T_2}{\partial r}\right)\,, \\ &\quad r > r_0\,, \end{aligned}\right\} \quad t > 0\,, \tag{30.8}$$

$$T_1 = T_2 = 0\,, \quad \text{when } t = 0\,, \tag{30.9}$$

$$\left.\begin{aligned} T_1 &= T_2 \\ \mu_1\frac{\partial T_1}{\partial r} &= \mu_2\frac{\partial T_2}{\partial r} \end{aligned}\right\} \quad \text{for } r = r_0\,, \tag{30.10}$$

$$T_1 \text{ finite as } r \to 0 \text{ and } T_2 \text{ finite as } r \to \infty\,. \tag{30.11}$$

Using the Laplace transformation for T, defined by

$$\overline{T} = \int_0^\infty \mathrm{e}^{-pt}T(t)\,\mathrm{d}t = L[T(t)]\,,$$

Eqs. (30.8–30.11) can be reduced to the stationary heat transfer equations

$$\left.\begin{aligned} \tfrac{\partial^2}{\partial r^2}\left(r\overline{T_1}\right) - rq_1^2\overline{T_1} &= -\tfrac{rA}{\mu_1 p}\,, 0 \le r < r_0\,, \\ \tfrac{\partial^2}{\partial r^2}\left(r\overline{T_2}\right) - rq_{21}^2\overline{T_2} &= 0\,, \quad r > r_0\,, \end{aligned}\right\}\,, \tag{30.12}$$

$$\left.\begin{aligned} \overline{T_1} &= \overline{T_2} \\ \mu_1\tfrac{\partial\overline{T_1}}{\partial r} &= \mu_2\tfrac{\partial\overline{T_2}}{\partial r} \end{aligned}\right\} \text{ for } r = r_0\,, \tag{30.13}$$

$$\overline{T_1} \text{ finite as } r \to 0 \text{ and } \overline{T_2} \text{ finite as } r \to \infty\,, \tag{30.14}$$

where $q_1^2 = p/\chi_1$ and $q_2^2 = p/\chi_2$.

The solution of (30.5–30.7) for the temperature distribution inside the heated sphere is [30.43]

$$\overline{T_1} = \frac{r_0^2 A}{\mu_1}\left\{\tfrac{1}{3}\tfrac{\mu_1}{\mu_2} + \tfrac{1}{6}\left(1 - \tfrac{r^2}{r_0^2}\right) - \tfrac{2r_0 b}{\pi r}\int_0^\infty \times \frac{\exp(-y^2 t/\gamma_1)}{y^2}\,\frac{(\sin y - y\cos y)\sin(ry/r_0)}{(c\sin y - y\cos y)^2 + b^2 y^2 \sin^2 y}\,\mathrm{d}y\right\}\,, \tag{30.15}$$

where

$$b = \frac{\mu_2}{\mu_1}\sqrt{\frac{\chi_1}{\chi_2}}\,, \quad c = 1 - \frac{\mu_2}{\mu_1} \quad \text{and} \quad \gamma_1 = \frac{r_0^2}{\chi_1}\,. \tag{30.16}$$

The temperature at the center of the sphere is

$$(\overline{T_1})_{r=0} = \frac{r_0^2 A}{\mu_1}\left\{\tfrac{1}{3}\tfrac{\mu_1}{\mu_2} + \tfrac{1}{6} - \tfrac{2b}{\pi}\int_0^\infty \frac{\exp(-y^2 t/\gamma_1)}{y} \times \frac{(\sin y - y\cos y)\sin(ry/r_0)}{(c\sin y - y\cos y)^2 + b^2 y^2 \sin^2 y}\,\mathrm{d}y\right\}\,, \tag{30.17}$$

and the temperature outside the sphere is

$$\overline{T_2} = \frac{r_0^3 A}{r\mu_1}\times \left\{\tfrac{1}{3}\tfrac{\mu_1}{\mu_2} - \tfrac{2}{\pi}\int_0^\infty \frac{\exp(-y^2 t/\gamma_1)}{y^3}\times \frac{(\sin y - y\cos y)[by\sin y\cos\sigma y - (c\sin y - y\cos y)\sin\sigma y]}{(c\sin y - y\cos y)^2 + b^2 y^2\sin^2 y}\,\mathrm{d}y\right\}\,, \tag{30.18}$$

with b, c, and γ_1 as in (30.16) and

$$\sigma = \left(\frac{r}{r_0} - 1\right)\sqrt{\frac{\chi_1}{\chi_2}}\,. \tag{30.19}$$

The heat source is characterized here by a constant rate A per unit time per unit volume as

$$A = \frac{E_{\mathrm{abs}}}{\tau_{\mathrm{rel}} V} = \frac{K_{\mathrm{abs}}\varepsilon_{\mathrm{L}} S}{\tau_{\mathrm{rel}} V}\,, \tag{30.20}$$

where E_{abs} is the energy absorbed by the nanoparticle, ε_{L} is the laser pulse energy density, K_{abs} is the absorption efficiency of the nanoparticle at the given wavelength of laser radiation, S and V are the area and volume of the absorbing center, and τ_{rel} is the thermal relaxation time in the biological medium. By using spherical symmetry for the absorbing center of radius r_0, we can reduce (30.20) to

$$A = \frac{3K_{\mathrm{abs}}\varepsilon_{\mathrm{L}}}{\tau_{\mathrm{rel}} r_0}\,. \tag{30.21}$$

The model described above can be used for simulating the spatial distribution of the temperature for a single or many heat sources in a cell volume.

30.5.2 Laser Heating of a Single Nanoparticle in Biomedia

Let us first calculate the laser heating of single gold nanoparticles with radii $r_0 = 30$–35 nm in water and surrounding blood biomedia when the incident laser pulse has an energy density of $E = 5\,\mathrm{J/cm^2}$ and pulse duration of $\tau_{\mathrm{L}} = 8$ ns. The laser flux is chosen at the level of $5\,\mathrm{J/cm^2}$ to provide cell lethality during a single laser pulse shot, being comparable to the laser fluence currently used in clinical treatments of pigmented skin lesions. The results of these simulations are presented in Figs. 30.11 and 30.12. Figure 30.11 illustrates the spatial behavior of the temperature inside 30 and 35 nm gold particles heated and cooled in the surrounding water and blood media. Figure 30.12 shows the spatial distribution of the temperature outside these nanoparticles.

The events that take place after absorption of the laser pulse energy by small particles depend on the size of the locally heated region and duration of laser exposure. Long pulses that exceed the thermal relaxation time in biological tissue, $\tau_{\mathrm{r}} = l^2/4\chi_{\mathrm{t}}$ (where χ_{t} is the thermal diffusivity of the biological tissue, and l is the minimum size of the locally heated region), cause heating of both the particle and the surrounding media. If the size of the locally heated region l is chosen to be equal to the size of the laser focal spot, which is about 1 μm, the thermal relaxation time for water is 1.75 μs and for blood is 1.56 μs, which is much longer than the laser pulse duration (≈ 10 ns) used in our research. For ultrashort laser pulses when $\tau_{\mathrm{L}} \ll \tau_{\mathrm{r}}$, the absorbed energy can be thermally confined within the target, causing rapid heating of the absorber itself. The extreme temperature rise in the absorber can induce ex-

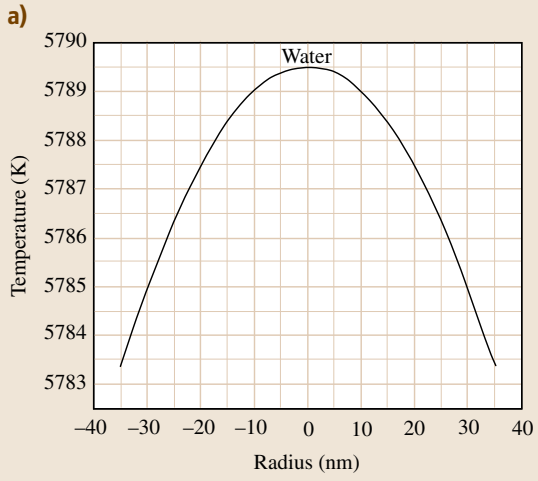

Fig. 30.11a,b One-dimensional distribution of the temperature inside a gold nanoparticle in surrounding water and blood media irradiated by a single laser pulse of energy density 5 J/cm^2 and duration 8 ns

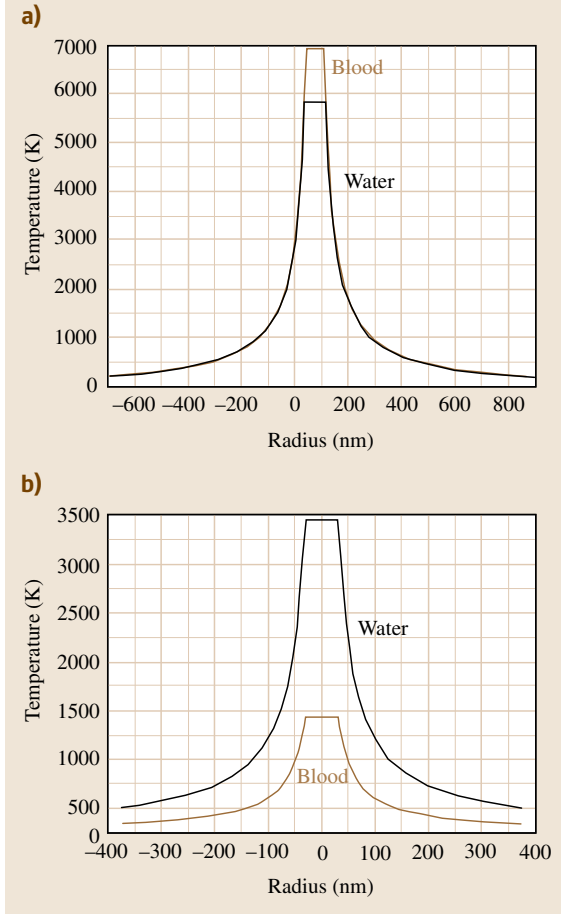

Fig. 30.12a,b Spatial distribution of the temperature outside the 30 nm gold particle **(a)** in surrounding water and blood media irradiated by a single laser pulse of energy density 5 J/cm^2 and duration 8 ns and **(b)** in a blood medium irradiated by a single laser pulse of energy density 2.5 J/cm^2 (*upper curve*) and 1 J/cm^2 (*lower curve*)

plosive vaporization of the nanoparticle, as described in the final section of this chapter.

Internal Temperature Distribution in a Single Nanoparticle

The integration of (30.15–30.17) gives the temperature distribution inside the heated nanoparticle surrounded by the biomedia. Our numerical simulations of the internal 30 nm gold particle's temperature distribution heated by a 5 J/cm^2 laser pulse of 8 ns width in the surrounding water and blood media show that the particle reaches its maximum temperature $T_{max} \approx 5789.5$ K in water and $T_{max} = 6870$ K in blood at the center of the sphere. Then we observe a small decrease of the inside temperature by 6 K to the particle's boundaries, establishing the stationary surface temperature of 5783.3 K in water and 6863.6 K in blood (Fig. 30.11). Since the temperature variation inside the nanoparticle occurs over a small range of 6 K, the internal particle's temperature can be assumed to be constant (Fig. 30.11b). Thus, the quasistationary and homogeneous approach can be applied to modeling the laser heating and evaporation of the nanoparticles in the biological media.

Table 30.8 Material properties of bone

Symbol	Property	Value	Reference
μ	Thermal conductivity	5.60×10^{-1} W/(m K)	[30.44]
ρ	Density	$1.85\times10^{+3}$ kg/m^3	[30.45]
c	Specific heat	$1.33\times10^{+3}$ J/(kg K)	[30.46]
χ	Thermal diffusivity	2.276×10^{-7} m^2/s	

Table 30.9 Material properties of gold

Symbol	Property	Value
μ	Thermal conductivity	$3.18\times10^{+2}$ W/(m K)
ρ	Density	$1.93\times10^{+4}$ kg/m^3
c	Specific heat	$1.29\times10^{+2}$ J/(kg K)
χ	Thermal diffusivity	1.276×10^{-4} m^2/s

Table 30.10 Material properties of silver

Symbol	Property	Value
μ	Thermal conductivity	$4.29\times10^{+2}$ W/(m K)
ρ	Density	$1.05\times10^{+4}$ kg/m^3
c	Specific heat	$2.35\times10^{+2}$ J/(kg K)
χ	Thermal diffusivity	1.74×10^{-4} m^2/s

Outside Temperature Distribution Around a Single Nanoparticle

As follows from Fig. 30.12, there is a significant heat loss from the surface of a nanoparticle to the surrounding medium, suggesting that even lower-energy pulses are enough to achieve true and large thermal damage of the biological surroundings. If the temperature of the surrounding medium exceeds some thermal thresholds, secondary phenomena of cell killing effects may develop, such as photothermal ablation, sound generation, bubble formation, and so on. For most cancer cell killing effects, the threshold temperature is about 150 °C (423 K). Calculations show that, at this level of the threshold temperature, the damage area produced by a heated 30 nm gold particle in blood has a size of ≈ 1 μm in diameter, which exceeds by 16 times the size of the nanoparticle (Fig. 30.12a). Thus, under chosen conditions, the damage area produced by one 30 nm particle heated by a single laser pulse of 5 J/cm^2 is comparable to the size of the laser focal spot.

To find the lowest energy level of the laser pulse required to achieve thermal thresholds for cell death, we have conducted calculations of the temperature spatial distribution of gold nanoparticles irradiated by different laser fluxes. The results of these simulations are illustrated in Fig. 30.12b. As follows from these calculations, a single 8 ns laser pulse of energy density 2.5 J/cm^2 provides heating of the 30 nm gold particle in the surrounding blood up to the boiling point of gold, ≈ 3400 K. The melting point of gold ≈ 1400 K is reached for a lower energy pulse density of 1 J/cm^2 for 8 ns laser pulse duration. Decreasing the energy density of the incident single laser pulse leads to a smaller damage volume around the nanoparticle. Using the threshold temperature of 423 K for cell death, we can determine the size of cell damage produced by the heated 30 nm gold particle. For the 8 ns single laser pulse with energy density of 2.5 J/cm^2, the damage volume around the nanoparticle has 0.5 μm diameter, which is smaller than but still comparable to the focal spot of the incident laser pulse. In the case of a 1 J/cm^2 single laser pulse, the damage area is 180 nm in diameter, which is only thrice the diameter of the nanoparticle. Thus, for experimental realization of selective nanophotothermolysis of cancer cells by a single 30 nm gold particle, we recommend use of a laser pulse with energy density 2.5 J/cm^2 for 8 ns width.

30.5.3 Bone Tissue Ablation by Plasmonic Nanoparticles

Both thermal and optical properties affect the behavior of the thermal field. The thermal properties of the material govern how easily a material can dissipate heat to the surrounding medium, while the optical properties govern how much heat is generated when exposed to an energy source. In these simulations we wish to examine the photothermal effect of a strongly absorbing nanoparticle in hard tissue for applications to medical procedures. For this reason, the material properties of bone and various nanoparticles are listed in Tables 30.8–30.10.

The optical properties of nanoparticles can be much more varied, however, as the absorption efficiency of the particles is affected by the material, size, and geometry of the nanoparticle. To achieve sufficient heating with pulses of lower energy densities, it is important to find absorption efficiency peaks. These peaks occur due to the plasmon resonance of the nanoparticle at that particular wavelength. To determine the ab-

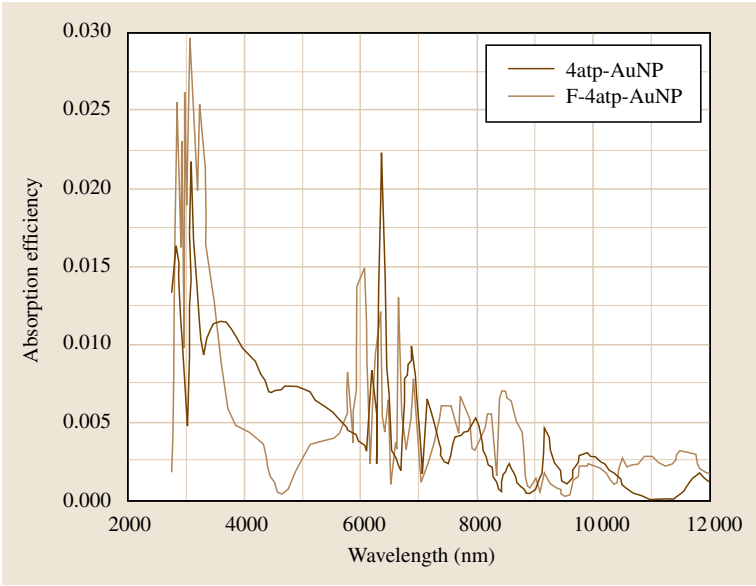

Fig. 30.13 Absorption efficiency for 5 nm aminothiophenol-conjugated gold nanoparticles (4atp-AuNP) and folate-aminothiophenol-conjugated gold nanoparticles (F-4atp-AuNP). The values are calculated with Mie theory using complex index of refraction data for gold from *Shakeri-Zadeh* et al. [30.47]

sorption characteristics of spherical particles in various biomedia, generalized Lorenz–Mie diffraction theory is used (Sect. 30.2), which takes into account the plasmon-resonance absorption effect. Using the complex indices of refraction for the medium and particle (which depend on the wavelength as well as particle size), the theory allows us to determine the absorption efficiency of spherical particles at any wavelength within the bounds of the refractive index values provided. The results of these calculations for the absorption efficiency of AuNP, AgNP, and CuNP are shown in Figs. 30.13 and 30.14 and are listed in Tables 30.1 and 30.2.

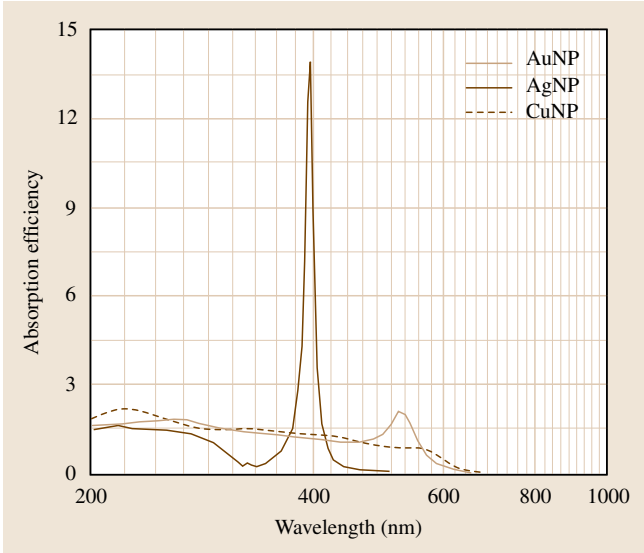

Fig. 30.14 Absorption efficiency for 30 nm-diameter gold, silver, and copper nanoparticles (AuNP, AgNP, CuNP) surrounded by water medium. These values are calculated with Mie theory using complex index of refraction data from *Johnson* and *Christy* [30.48]

Reduction in the size of the spherical nanoparticles lowers the absorption efficiency, as seen when comparing 30 to 5 nm AuNP, where K_{abs} loses an entire order of magnitude. Moving into the IR and

Table 30.11 Parameters for AuNP heating simulation achieving the critical heat of vaporization for bone at the nanoparticle edge

Symbol	Property	Value
d	Nanoparticle diameter	30 nm
E	Pulse energy density	0.788 J/cm^2
λ	Wavelength	520 nm
K_{abs}	Absorption efficiency	2.1

Table 30.12 Parameters for AgNP heating simulation achieving the critical heat of vaporization for bone at the nanoparticle edge

Symbol	Property	Value
d	Nanoparticle diameter	30 nm
E	Pulse energy density	0.119 J/cm^2
λ	Wavelength	394 nm
K_{abs}	Absorption efficiency	13.9

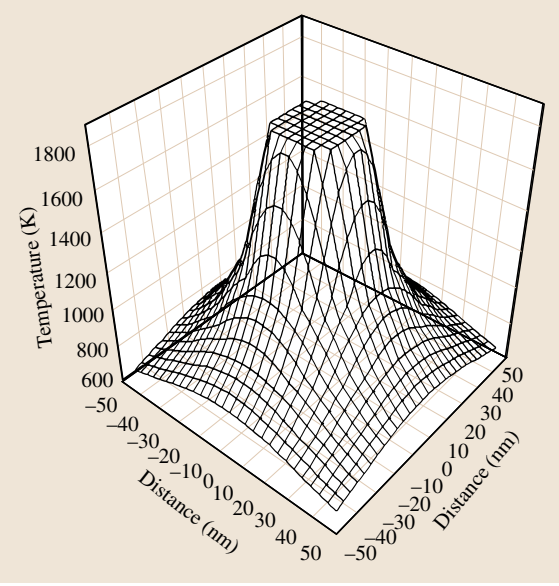

Fig. 30.15 The spatial distribution of the temperature for a 30 nm-diameter Au nanoparticle heated up to the critical temperature of bone vaporization. The simulation parameters are listed in Table 30.11

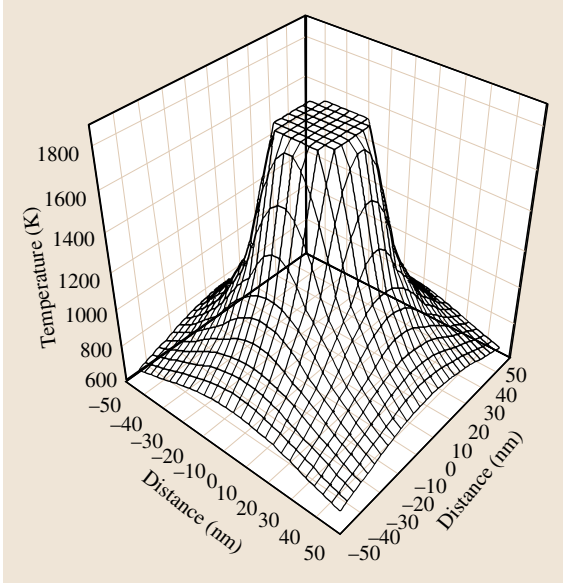

Fig. 30.16 The spatial distribution of the temperature for a 30 nm-diameter Ag nanoparticle heated up to the critical temperature of bone vaporization. The simulation parameters are listed in Table 30.12

longer wavelengths, the absorption efficiency decreases continuously and without any noticeable peaks upon which to capitalize. This means that larger energy densities would be required to heat the nanospheres to the critical temperature. Thus, utilization of silica–gold nanoshells and/or gold nanorods, which absorb IR wavelengths much better than solid nanospheres, is recommended for selective nanothermolysis of bone tissue when working in the longer-wavelength range of the spectrum.

The choices of nanoparticle material, size, and shape used in the model are listed in Tables 30.11 and 30.12 along with the choice of wavelength and corresponding absorption efficiency for that wavelength. The energy densities were chosen to bring the nanoparticle to the melting temperature of hydroxyapatite (1843 K) [30.48] as it is the main constituent of bone tissues. This was considered an appropriate choice for the ablation temperature, as *Fried* et al. showed thermal ablation and expulsion of molten drops in the temperature range of 1473–2273 K [30.49].

The temperature distribution is mainly dependent upon two factors: the thermal conductivities, which affect the slopes of the curves, and the absorption efficiency, which affects the maximum temperature difference reached. In the case of noble-metal nanopar-

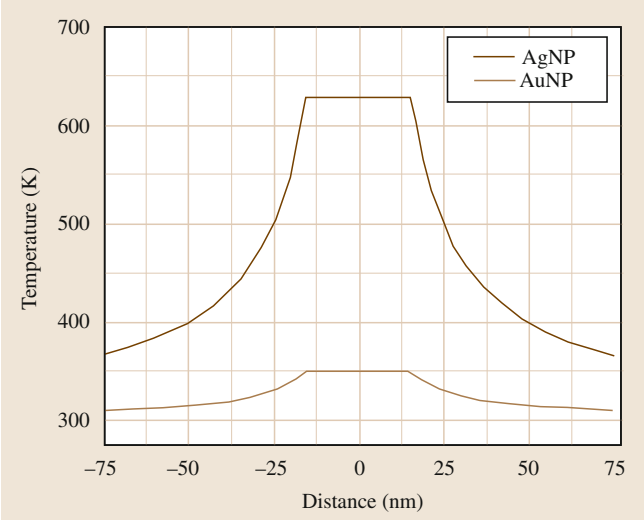

Fig. 30.17 Heat profiles for a 30 nm-diameter AgNP (*solid curve*) heated by a $\lambda = 394$ nm pulse, and a 30 nm-diameter AuNP (*dotted curve*) heated by $\lambda = 520$ nm. Both pulses have equivalent energy densities, and both spheres are within an infinite medium with steady-state temperature 300 K ▶

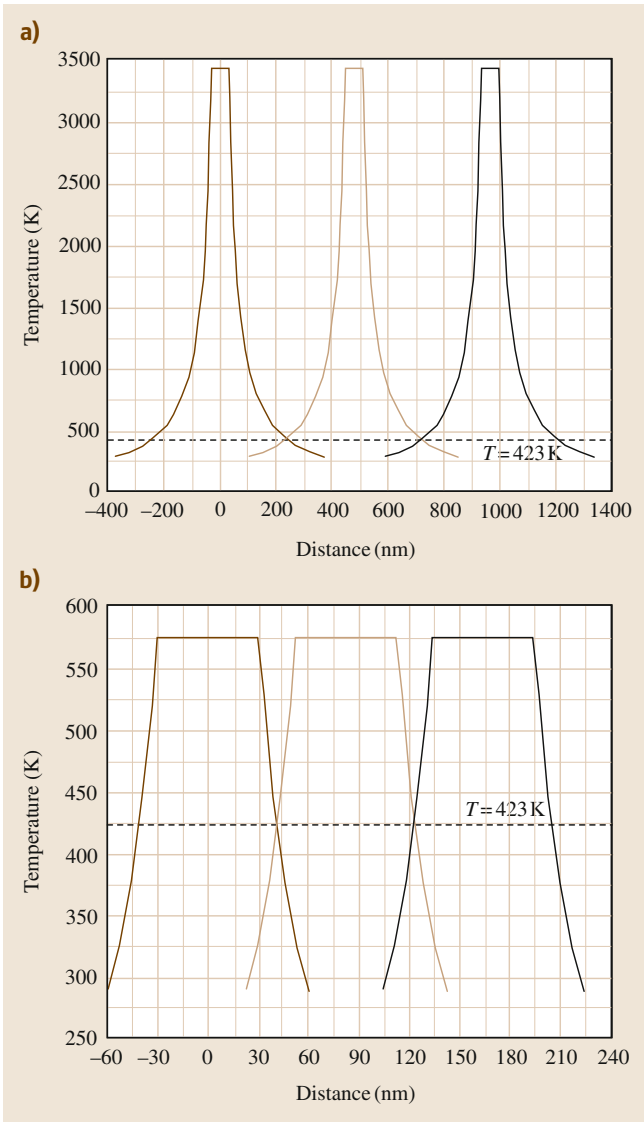

Fig. 30.18a,b Spatial distribution of the temperature fields produced in the blood medium **(a)** by many heat sources irradiated by a single laser pulse with energy density of 2.5 J/cm^2 and pulse duration 8 ns, and **(b)** inside a cluster consisting of 30 nm gold particles irradiated by a 8 ns single laser pulse of energy density 0.42 J/cm^2

ticles, the thermal conductivities of the metals are more than two orders of magnitude greater than that of bone. This leads to an essentially homogeneous temperature distribution within the nanoparticle, with an exponential cooling outside the particle as shown in Figs. 30.15–30.17.

In Fig. 30.17, it is clear that temperature is essentially the same within the nanoparticle radius, with significant cooling outside the radius. Closer inspection shows that the temperature distribution on the plateau varies slightly from the hottest point at the center, to the coolest temperature at the nanoparticle edge. For AgNP this is a variance from 628.1 to 627.8 K, and for AuNP it varies from 349.6 to 349.5 K. Both show less than 0.1% variance from the maximum temperature, and thus the plateau regions can be considered homogeneously heated.

Outside the nanoparticle, the temperatures drop relatively rapidly. In Figs. 30.15 and 30.16 for example, hard-tissue temperatures at the edge of the nanoparticle are at the hydroxyapatite melting temperature (1843 K) and maintain a temperature above 1473 K at a distance 1.05 times the radius of the nanoparticle (i. e., a 31.5 nm-diameter area is heated to this level by the 30 nm nanoparticle). This temperature is the lower bound (1473–2273 K) shown by Fried et al. to produce hydroxyapatite ablation and expulsion of molten drops. The temperature for delayed thermal necrosis of osteocytes (320 K) is maintained for all the tissue up to 75 times the radius, making the cell damage area on the same order of magnitude as the focal spot size.

Thus, we have discussed the method of selective nanophotothermolysis for application to bone tissue cancers. Our simulations for three-dimensional (3-D) thermal fields of plasmonic nanoparticles surrounded by bone medium have shown that alterations to the particle size, particle shape, and material all have effects on the magnitude of the maximum temperature reached in the particle; For example, in the UV and visible ranges of the spectrum, silver and gold solid spherical nanoparticles exhibit a strong plasmonic effect in laser heating of nanoparticles. For longer wavelengths in the transparency window of most biotissues, we recommend utilization of silica–gold nanoshells and/or gold nanorods for selective nanothermolysis of the bone tissue. Additionally, heat loss from the surface of a nanoparticle to the surrounding medium is observed, creating a large thermal damage area in the bone tissue up to 75 times the nanoparticle radius.

30.5.4 Temperature Simulations for Many Heat Sources

The model of (30.15–30.21) can be used for simulations of the spatial distribution of the temperature produced by many heat sources. Figure 30.18a illustrates the temperature fields around closely located nanoparticles in

the surrounding blood medium irradiated by a single laser pulse with energy density of 2.5 J/cm^2 and pulse duration of 8 ns. As follows from these calculations, to provide the threshold temperature 423 K between the particles everywhere in the cell volume (i. e., thermal damage in the cell), the interparticle distance l (i. e., between the centers of neighboring nanoparticles) should not exceed $l \leq 480$ nm.

This criterion can be reached by varying l and the energy density of the incident laser pulse. To find the optimal distance l, where the minimal temperature between the nanoparticles is equal to 423 K, we have conducted calculations of the interparticle temperature distribution for different values of the laser energy density. Results of these simulations, presented in Fig. 30.19, show that an optimum l does not exist in the framework of the thermal calculations: l linearly increases with the energy density of the incident laser pulse. The interparticle distance l sets the lower limit for the nanoparticle concentration n required for cell death (i. e., the number of particles per unit volume) as

$$n = \left(\frac{1}{l^3}\right) . \tag{30.22}$$

Let us estimate n and the absolute number N of nanoparticles to provide the high-temperature distribution inside the cancer cell volume. For $l = 480$ nm, the concentration of $n = 9.0 \times 10^{12}$ cm^{-3} is homogeneously distributed throughout the cell volume. N can be found as $N = nV_{\text{cell}}$, where V_{cell} is the cell volume. In the case of the 10 μm-diameter cells of the MDA-MB-231 breast cancer line, the number of 30 nm gold particles needed to provide the threshold temperature everywhere

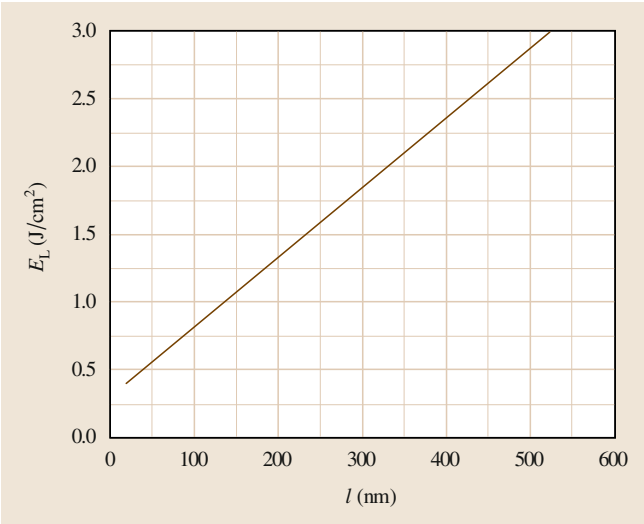

Fig. 30.19 Interparticle distance for different values of the laser energy density

in the cell volume (thermal damage) is $N \approx 4710$. This is a relatively large number of particles per cell, requiring a long incubation time to collect them in the cell or cell membrane. As shown in our experiments [30.12], during this incubation time, the nanoparticles collide with each other, stick together, and form nanoparticle clusters. The temperature distribution inside a cluster is expected to be significantly higher than the threshold temperature 423 K, since the particles in the cluster are compacted much closer to each other. The spatial distribution of the temperature field inside and outside the cluster formed by 30 nm particles conjugated with antibodies is shown in Fig. 30.18.

30.6 New Dynamic Modes in Selective Plasmonic Nanotherapy

30.6.1 Nanocluster Aggregation Mode

Under certain delivery and particle-accumulation conditions, nanoparticles can form clusters in the cancer cell volume or cell membrane surface, as shown in Fig. 30.20. A cluster is a group of closely located nanoparticles (10–30 nm each) separated by the thickness of antibodies with total cluster size of 200–400 nm, which depends on the radii of the nanoparticles and duration of incubation time. This is the time required to collect the appropriate number of nanoparticles in the cell or cell membrane. The presence of nanoclusters may provide further synergistic enhancement of selective nanophotothermolysis due to:

- Increase of the nanocluster's average local absorption
- Red-shifting of absorption to the near-IR range (window of transparency of most biotissues [30.26]) that may be achieved with conventional gold solid nanospheres, which are simpler to prepare, stable, and nontoxic, and cheaper compared with nanoparticles with special design (e.g., rods, shells, etc.)

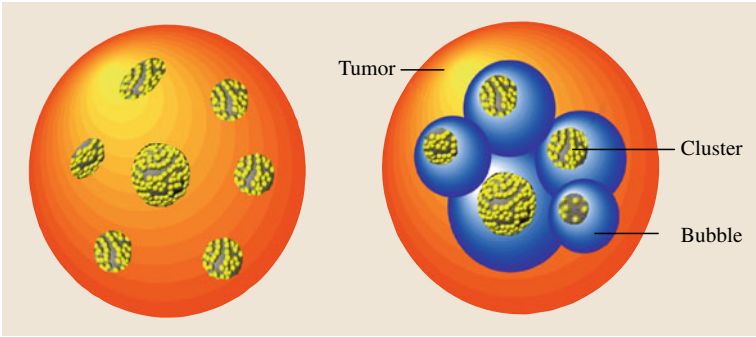

Fig. 30.20 Principle of the nanocluster aggregation mode in selective nanophotothermolysis of cancer

- Better heating efficiency achieved
- Decrease in threshold energy for bubble formation and cell damage.

In this section, we describe theoretically the damage of abnormal cells produced by nanoclusters and then compare this with the single-particle case. Two basic mechanisms of killing of cancer cells in the cluster aggregation mode (CAM) corresponding to a nanosecond laser pulse duration are studied here: thermal damage of abnormal cells by a laser-heated cluster, and bubble generation and their overlapping around the nanoparticles/nanocluster, as shown in Fig. 30.20.

Temperature Distribution Inside the Nanocluster

Our experiments [30.12] show that the distance between the centers of neighboring particles in a cluster is 80 nm, i. e., 20 nm between the surfaces of 30 nm particles. The interparticle distance in the cluster cannot be less than 20 nm, since the particles are covered by antibodies with thickness of about 10 nm. The model described in Sect. 30.4 is used to calculate the temperature distribution inside the cluster consisting of separate gold nanoparticles with radius $r_0 = 30\,\text{nm}$ in the surrounding blood medium irradiated by a single laser pulse of energy density $E = 2.5\,\text{J/cm}^2$ and pulse duration $\tau_\text{L} = 8\,\text{ns}$. As follows from these calculations, the $2.5\,\text{J/cm}^2$ single laser pulse provides an extremely high minimal temperature of 2574 K inside the cluster (minimal temperature between the nanoparticles). The surface temperature of the nanoheaters is 3432 K. So, at the same energy level of the incident laser radiation used for laser heating of the single nanoparticle, the minimal temperature inside the cluster exceeds by six times the threshold temperature for cell killing. Thus, the aggregation of the nanoparticles in clusters gives us a unique possibility to dramatically decrease the incident laser pulse energy with the same efficiency of cell death.

To find the lowest energy level of the incident single laser pulse, we have conducted calculations of the spatial distribution of the temperature inside a cluster consisting of 30 nm gold particles for different laser fluxes. The size of the cluster is chosen to be smaller than that of the laser focal spot. The results of these simulations for the lowest energy providing the threshold temperature of not less than 423 K inside the cluster (between nanoparticles) are illustrated in Fig. 30.18b. As follows from these calculations, an 8 ns single laser pulse with energy density of $0.42\,\text{J/cm}^2$ is enough to heat the 30 nm gold particles inside the cluster up to 577 K and to reach the minimal temperature of 432 K in the cluster volume. There is evidence that specific properties of gold nanoparticles may be the reason for the remarkably low melting temperature (573 K) [30.50]. Thus, clusters aggregated from small nanoparticles can provide thermal damage of cancer cells at the significantly low energy level of $0.42\,\text{J/cm}^2$ of the incident single laser pulse.

Temperature Distribution Outside the Nanocluster

We assume that the cluster is aggregated from 30 nm gold particles with 20 nm interparticle distances, homogeneously compacted in a cylinder of length 380 nm. The cluster is located along the r-axis and surrounded by blood. It is irradiated by a single laser pulse of energy density $1\,\text{J/cm}^2$ and pulse duration of 8 ns at full-width at half-maximum (FWHM). Results of the simulations for the spatial distribution of the temperature field inside and outside the cluster in the surrounding blood medium are displayed in Fig. 30.21a. As follows from these calculations, the temperature inside the cluster oscillates in the range of 1374–1056 K along its length. So, the cluster heated by a single laser pulse of energy

density $1\,J/cm^2$ has a high inside temperature which exceeds by thrice the threshold temperature for cell death. The outside temperature distribution shows us that the cluster provides a large thermal damage area of $\approx 0.5\,\mu m$ within the cell volume at the threshold temperature level of 423 K. To reach the same thermal damage area with a single nanoparticle, a laser pulse with energy density 2.5 times higher than for the cluster case is required.

We note that, since the cluster is treated here as a discrete medium (each particle considered separately), the results obtained above for the cluster temperature and thermal damage area have their lowest values. The upper limit for these values can be found for a homogeneous (continuous) distribution of the medium in the cluster. To keep our notations here the same, we label such a continuously distributed medium as a homogeneous cluster. There are two reasons in support of the homogeneous distribution in the cluster.

The first is the optical area. The size of nanoparticles in a cluster is much smaller than the wavelength of the laser radiation, $r_0 \ll \lambda$. As shown in [30.1], according to the Lorenz–Mie scattering theory, the cross-section of absorption exceeds by four times the geometric cross-section of the gold nanoparticle, $\sigma_{abs} > \sigma_0$. Hence, cross-sections of absorption of each nanoparticle are overlapping in the cluster. Because of this, the light does not distinguish the separate nanoparticles inside the cluster, and the laser energy is distributed homogeneously among the particles.

The second reason is the heat transfer frame. Since the temperature variation inside the nanocluster occurs over a relatively small temperature range of 318 K (45 °C), we can assume that the internal cluster temperature is homogeneous and constant. This means that, from a thermal calculations point of view, the cluster can be treated as homogeneous (continuous) gold particles with the same size.

Let us evaluate the damage area produced by continuous gold *clusters* in the blood medium. The temperature distribution for gold particles of radius 190 nm (cluster diameter 380 nm) in blood irradiated by a single laser pulse of energy density $1\,J/cm^2$ is illustrated in Fig. 30.21b. As follows from these simulations, the upper limit of temperature inside the homogeneous cluster is 2384 K, and the thermal damage area is $2.13\,\mu m$ in diameter at the threshold temperature level of 423 K. Thus, the 380 nm cluster provides a huge thermal damage area with minimum size of $0.5\,\mu m$ (for a discrete cluster) up to a maximal size of $2\,\mu m$ (for a homogeneous cluster) in a cell volume irradiated by a single laser pulse of energy density $1\,J/cm^2$.

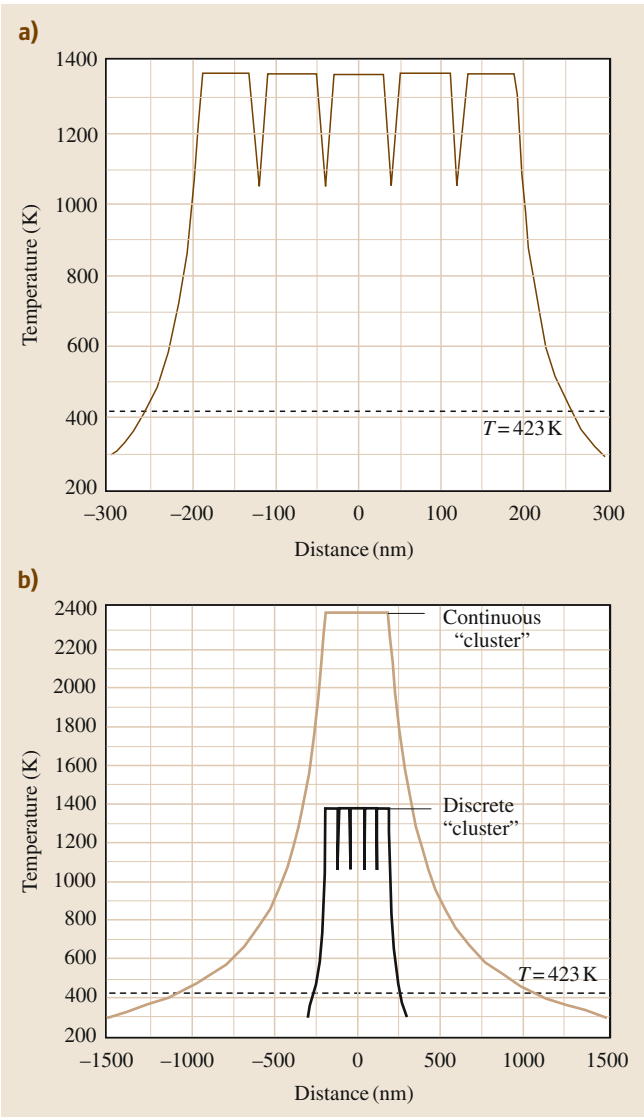

Fig. 30.21a,b One-dimensional distribution of the temperature field inside and outside a discrete cluster **(a)** and continuous cluster **(b)** consisting of 30 nm gold particles in the surrounding blood medium irradiated by a single laser pulse of energy density $1\,J/cm^2$

On the basis of our theoretical modeling, we can conclude that the aggregation of nanoparticles in a cluster mode of nanophotothermolysis raises the efficiency of cancer cell treatment due to the large damage area at

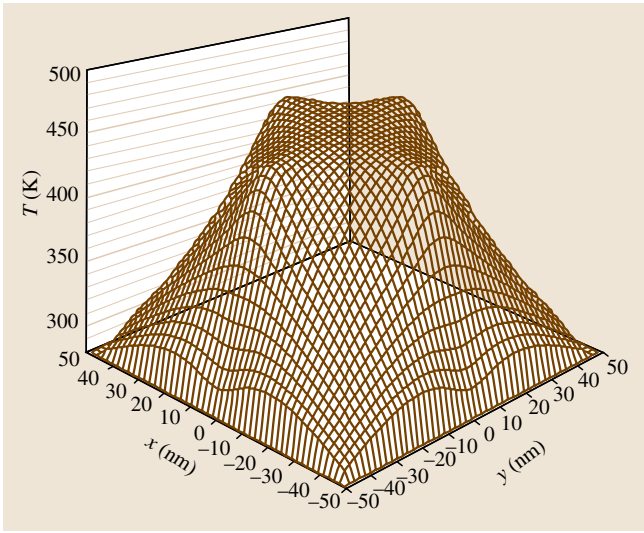

Fig. 30.22 Two-dimensional distribution of the temperature inside and outside a 30 nm gold nanoparticle in surrounding water and blood media irradiated by a single laser pulse of energy density $0.33\,\mathrm{J/cm^2}$ and duration 8 ns

relatively low energy density of the incident single laser pulse. This conclusion is supported by the following results:

- The same laser energy density used for heating a single nanoparticle to the minimal temperature for thermal cell damage provides a temperature six times greater inside the cluster.
- Clusters can produce thermal damage of cancer cells at a significantly lower energy density level of $0.42\,\mathrm{J/cm^2}$ of the incident single laser pulse in comparison with a single particle.
- Clusters provides a larger thermal damage area with minimal size of 0.5 μm (for the discrete cluster case) up to maximal size of 2 μm (for a continuous *cluster*) in a cell volume irradiated by a single laser pulse of energy density $1\,\mathrm{J/cm^2}$ and duration of 8 ns. To reach the same thermal damage area of 0.5 μm by a single nanoparticle, a laser pulse with energy density 2.5 times higher than for the cluster case is required.

We should note that the damage area is estimated here by using the threshold temperature required for the initiation of cell killing effects, i. e., thermal damage. However, the actual damage area is expected to be significantly larger since the damage can occur on the cellular level, for example, due to bubble formation around the nano-absorbers and its expansion in the cell volume. Section 30.5.2 is devoted to the investigation of the microbubble dynamics around nanoparticles/nanoclusters in biological media.

30.6.2 Microbubble Overlapping Mode

As shown in Sect. 30.5.1, significant heat conduction away from a heated nanoparticle requires timescales of the order of microseconds (1.75 μs for water and 1.56 μs for blood). Because of this, for nanosecond laser pulses, most of the pulse energy remains localized at the absorbing nanoparticles/cluster, whose temperature rises high enough to cause vaporization of the immediate surrounding medium. This creates a bubble that then expands outward from the nanoparticle. We now investigate the bubble dynamics resulting from laser pulses with duration of 8 ns at FWHM.

Experiments [30.12] show that it is enough to heat the strongly absorbing nanoparticles above the boiling temperature of water only, or above the critical temperature of the phase transition in water, to generate bubbles around the particles. So, for a relatively low laser flux, the nanoparticle will be surrounded by a rapidly expanding layer of vapor. Let us calculate the threshold energy density of laser pulse deposited into the nanoparticle which is required to raise its surface temperature to the level of the critical temperature for bubble generation.

An experimental nucleation temperature of $T_{\mathrm{thr}} = 150\,^{\circ}\mathrm{C}$ (423 K) for heterogeneous bubble generation on the melanosome's surface was determined by *Kelly* [30.51]. Our calculations (Fig. 30.22) show that a threshold energy density of $0.33\,\mathrm{J/cm^2}$ for the single 8 ns laser pulse is required to reach a surface temperature of 450 K for the 30 nm gold nanoparticles in blood medium. Thus, the bubble mode of photothermolysis can provide a larger damage area at the relatively low optical flux of $0.33\,\mathrm{J/cm^2}$ ($\tau_{\mathrm{L}} = 8$ ns) due to the rapidly expanding nanobubbles around the nanoparticles.

Spherical Bubble Dynamics

Consider a spherical bubble of radius $R(t)$ (where t is time) in an infinite domain of liquid whose temperature and pressure far from the bubble are T_∞ and $p_\infty(t)$, respectively. We will assume that the liquid density ρ_{L} and dynamic viscosity η_{L} are constant and uniform. It will also be assumed that the contents of the bubble are homogeneous, and that the temperature $T(t)$ and pressure $p(t)$ within the bubble are always uniform. The radius of the bubble will be one of the primary

results of the analysis. In the absence of mass transport across the boundary (evaporation or condensation) and with the above assumptions, the bubble dynamics can be described by the generalized Rayleigh–Plesset equation [30.52]

$$\frac{p_V(T_\infty)-p_\infty(t)}{\rho_L}+\frac{p_V(T)-p_\infty(T_\infty)}{\rho_L}+\frac{p_G}{\rho_L} = R\frac{d^2R}{dt^2}+\frac{3}{2}\left(\frac{dR}{dt}\right)^2+\frac{4\eta_L}{\rho_L R}\frac{dR}{dt}+\frac{2S}{\rho_L R}, \tag{30.23}$$

where $p_V(T)$ is the saturated vapor density, and p_G is the partial pressure of the contaminant gas contained in the bubble. The first term on the left side of this equation is the instantaneous tension, or driving term, determined by the conditions far from the bubble. We refer to the second as the thermal term. It will be assumed here that the behavior of the gas in the bubble is polytropic, so that

$$p_G = p_{G_0}\left(\frac{r_0}{R}\right)^{3k}, \tag{30.24}$$

where p_{G_0} is the partial pressure of the contaminant gas contained in the bubble at some reference size $R = r_0$, with k as approximately constant. Clearly, $k = 1$ implies a constant bubble temperature, and $k = \gamma$ would model adiabatic behavior, where γ is the ratio of the specific heat of the vapor at constant pressure to the specific heat at constant volume.

Equation (30.23) can be readily integrated numerically to find $R(t)$ and the rate of bubble growth $v = dR/dt$ given the input $p_\infty(t)$, the temperature T_∞, and the other constants. Initial conditions are also required and, in the context of cavitating flows, it is appropriate to assume that a nanobubble of radius $R = r_0$ is in equilibrium at $t = 0$ in the fluid at a pressure $p_\infty(0)$, so that

$$p_{G_0} = p_\infty(0) - p_V(T_\infty) + \frac{2S}{r_0} \tag{30.25}$$

and $(dR/dt)_{t=0} = 0$.

Overlapping Microbubbles

As discussed above, under certain delivery and particle-accumulation conditions, the particles can locate on the membrane surface very close to each other, as shown in Fig. 30.20. In this mode, we can expect the optical, thermal, acoustic, and bubble formation phenomena initiated by laser radiation around each particle to overlap and create some synergistic effects [30.12]; For example, the characteristic radii for these overlapping effects can be defined by an optical radius $R_{opt} = (\sigma_{abs}/\pi)^{1/2}$, thermal diffusion length $R_T = (kt)^{1/2}$, sound transfer distance $R_{ac} = c_s t$, and microbubble radius $R_{bubble} = v_b t$, where σ_{abs} is the cross-section of absorption, k is the heat diffusion coefficient, c_s is the speed of sound, and v_b is the bubble growth velocity. Since for a certain range of gold nanoparticle sizes the optical radius can exceed the geometrical particle radius r_o at the given wavelength of laser radiation, a plasmon–plasmon resonance at $R_{opt} > L$ (where L is the distance between particles) can be achieved. This resonance leads not only to the known *red-shifting* of maximum absorption [30.53], but also increases the integrated absorption coefficient of the particle cluster. The overlapping thermal fields at $R_T > L$ (during or after the laser pulse t_p) lead to a dramatic increase in thermal and accompanying effects (e.g., to sudden appearance of different nonlinear effects such as phase transitions). The interaction of acoustic waves at $R_{ac} > L/2$ significantly changes the local refractive index, which might be crucial for diagnostic purposes. Finally, the interaction of growing bubbles (initially of nanoscale sizes) at $R_{bubble} > L/2$ leads to a substantial increase in the average bubble size, with a decrease in the bubble-formation threshold (which, for single nanoparticles, is relatively high), and probably an increase in the bubble growth velocity. All of these phenomena are crucial when changing the distance between nanoparticles, and they are important for both highly sensitive diagnostics and efficient therapy.

We focus here on therapeutic application of this technology. Indeed, laser-induced overheating effects around nanoparticles may create many therapeutic actions through the microbubble formation phenomena, accompanied by acoustic and cavitation effects, mechanical stress, and laser-induced hydrodynamic pressure arising from the rapid bubble expansion and collapse. In this section, we discuss a dynamic mode for selective cancer treatment by laser-activated nanoheaters, involving the situation where the bubbles are overlapping inside the cell volume. The bubble overlapping mode (BOM) may dramatically increase the efficiency of the cancer treatment by laser-heated nanoparticles as a result of the large damage range.

Since bubbles do not all appear simultaneously, there are few possibilities for bubbles overlapping. The bubbles can overlap at different nucleation times and spreading velocities, or simultaneously with the same spreading velocity when they reach each other midway between neighboring gold particles. In our calculations, we choose stronger criteria than overlapping at

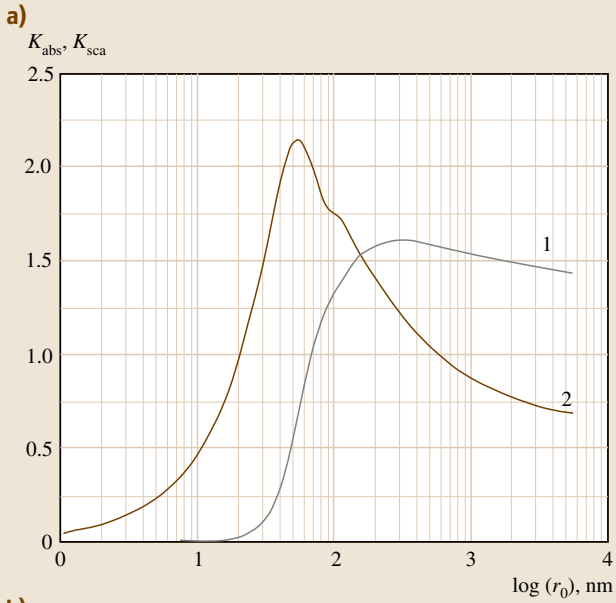

Fig. 30.23a,b Dependences of the scattering K_{sca} (*curve 1*) and absorption K_{abs} (*curve 2*) coefficients at laser wavelength of $\lambda = 450\,\text{nm}$ on the size r_0 of gold particles in water medium ($\tilde{m} = 1.122 - 1.416\,\text{i}$) **(a)** and **(b)** for the case $\lambda = 633\,\text{nm}$ ($\tilde{m} = 0.1126 - 2.5754\,\text{i}$) ◀

midpoints. Effective overlapping with large damage of tumor cells can be achieved if each bubble reaches the neighboring nanoparticles themselves, not just the midpoints between nanoparticles.

Condition for Concentration of Nanoparticles

The criteria for BOM introduced above impose a requirement on the interparticle distance L, the distance between two neighboring nanoparticles. Since the bubble must reach the neighboring particles during the growing time τ_{growth}, the integration of the Rayleigh–Plesset equation (30.23) [30.52] for bubble dynamics at the nucleation temperature T_{nuc} gives the requirement for the interparticle distance L as

$$L \le \sqrt{\frac{2}{3}\frac{P_{sat}(T_{nuc}) - P_\infty}{\rho(T_\infty)}}\,\tau_{growth}\,, \qquad (30.26)$$

where $P_{sat}(T_{nuc})$ is the saturated vapor pressure at the nucleation temperature, P_∞ is the ambient pressure, and $\rho(T_\infty)$ is the water density. This sets the lower limit to that required for the BOM concentration of nanoparticles, the number of particles per unit volume, as

$$n = (1/L^3)\,. \qquad (30.27)$$

Let us now estimate the interparticle distance, the nanoparticle concentration, and their absolute number collected in a tumor cell to provide the BOM by laser-activated nanoheaters. The interparticle distance L calculated by (30.26) for the experimentally measured nucleation temperature of $T_{nuc} = 150\,^\circ\text{C}$ is

$$L \approx 15.8\tau_{growth}\,. \qquad (30.28)$$

The bubble growing time τ_{growth} is limited by the bubble nucleation time t_{nuc} and bubble lifetime τ_{bubble}, i. e., $t_{nuc} \le \tau_{growth} < \tau_{bubble}$. In our experiments [30.12], the nucleation time of the bubbles around isolated gold nanoparticles in aqueous suspension and irradiated by nanosecond laser pulses is $t_{nuc} \approx 100\,\text{ns}$. The bubble lifetime depends on the laser energy and ranges from 100 ns to 2 µs. In the overwhelming majority of experiments, including ours, the bubble lifetime is in the range $\tau_{bubble} = 200–400\,\text{ns}$. So, we can conclude that the bubble growing time is close to the nucleation time, i. e., $\tau_{growth} \sim t_{nuc}$. Then, from the rate equation (30.28), we can estimate the distance between nanoparticles (microbubble radius) required for the BOM as $L = R_{bubble} \approx 1.6\,\mu\text{m}$, which corresponds to the results of our experiments. Thus, (30.27) gives the lower limit of the concentration of nanoparticles to provide the BOM as $n \approx 2.44 \times 10^{11}\,\text{cm}^{-3}$. The absolute number of particles homogeneously distributed inside a tumor cell

Table 30.13 Physical properties of blood at 1 atm pressure used in the simulations

Property	Notation used in the model	Value	Units
Density	ρ_L	998.2	kg/m^3
Viscosity (water)	η_L	1.022×10^{-4}	$kg\,s/m^2$
Surface tension (water-saturated vapor)	S	7.2×10^{-3}	kg/m
Thermal conductivity at $T = 273–373$ K	μ_0	0.48–0.6	W/(m K)
Thermal diffusivity	χ	1.6×10^{-7}	m^2/s
Specific heat at $T = 273–373$ K	c	3645–3897	J/(K kg)
Ratio of specific heats (water/vapor)	γ	1.33	

for this mode can be found as $N = nV_{cell}$, where V_{cell} is the cell volume. For the case of the breast cancer line MDA-MB-231 of 15 μm size, the number of gold nanoparticles providing BOM is $N \approx 430$.

Condition on Nanoparticle Sizes

The optimal range of nanoparticle sizes for effective laser initiation of BOM in tumor cells is governed by the nanoparticle optics described in [30.1]. The optical characteristics of spherical nanoparticles dispersed in a biological medium at a given radiation wavelength λ can be calculated on the basis of Lorenz–Mie diffraction theory in the single scattering approximation discussed in Sect. 30.2. The Mie formalism requires the use of two dimensionless input parameters, $\rho = 2\pi r_0/\lambda$ and $\delta = \rho\tilde{m}$, where $\tilde{m}$ is the relative value of the complex refractive index of the nanoparticles in the surrounding medium at the wavelength λ. Computer calculations of the dependences of the absorption K_{abs} and scattering K_{sca} coefficients at the given laser wavelength on the size of gold nanoparticles in aqueous suspension are plotted in Fig. 30.23. Figure 30.23a shows results for gold particles in water heated by laser radiation of wavelength $\lambda = 450$ nm ($\tilde{m} = 1.122–1.416\,i$), and Fig. 30.23b is for the case of wavelength $\lambda = 633$ nm ($\tilde{m} = 0.1126–2.5754\,i$). It is evident from Fig. 30.23a that the absorption coefficient K_{abs} has a strong maximum at the radius of 50 nm for the gold particle at the given wavelength (for 532 nm wavelength, the maximum radius is 30 nm).

The width of the absorption maximum at the level $K_{abs} \geq 1$ corresponds to the particle radii range of $r_0 = 20–600$ nm. This means that, in this size range, the absorption cross-section of gold particles at the given wavelength $\lambda = 450$ nm exceeds the particle geometric cross-section. Light scattering at $\lambda = 450$ nm by gold nanoparticles in aqueous suspension becomes apparent for particle radii larger than 50 nm. For particles of radii $r_0 \geq 150$ nm, the scattering of laser radiation predominates over the absorption, and the considered suspension containing the nanoparticles becomes a strongly scattering medium at the given wavelength.

For the particle radius range $r_0 = 1–50$ nm, the absorption coefficient K_{abs} is considerably greater than the scattering coefficient K_{sca}; i. e., the efficiency of laser heating of nanoparticles in this size range is high. Thus, the optimal range of nanoparticle sizes for effective laser initiation of BOM in tumor cells is 1–50 nm. The maximal effect of laser heating of gold particles can be achieved for particles of radii 20–50 nm, where $K_{abs} \geq 1$ and $K_{sca} < 1$.

Figure 30.23b demonstrates the $K_{sca}(r_0)$ and $K_{abs}(r_0)$ curves for the wavelength of $\lambda = 633$ nm. We observe very weak absorption and strong scattering of the light at this wavelength by the gold nanoparticles. The absorption slightly predominates over the scattering for a small range of nanoparticle radii when $r_0 \leq 35$ nm. It follows that laser light with wavelength $\lambda = 633$ nm can be recommended for diagnostic purposes only. However, creation of nanoclusters on a cell surface may lead to shifting the absorption maximum to the near-IR range [30.53], which can also be used for therapeutic purposes.

Thus, the proposed theoretical model for the nanoparticle optics along with bubble dynamics allows us to find the following conditions for BOM realization:

- The maximal effect of laser heating of gold nanoparticles over the wavelength range $\lambda = 450–550$ nm can be achieved for particle radii of 20–50 nm.
- The optimal nanoparticle concentration is $n \approx 2.44\times10^{11}\ cm^{-3}$, which corresponds to an absolute number of nanoparticles in a breast cancer cell volume of 430 (88 on the cell surface).
- The bubble radius providing BOM is $R_{bubble} \approx 1.6$ μm.

These theoretical predictions of the BOM conditions have been confirmed by our experimental re-

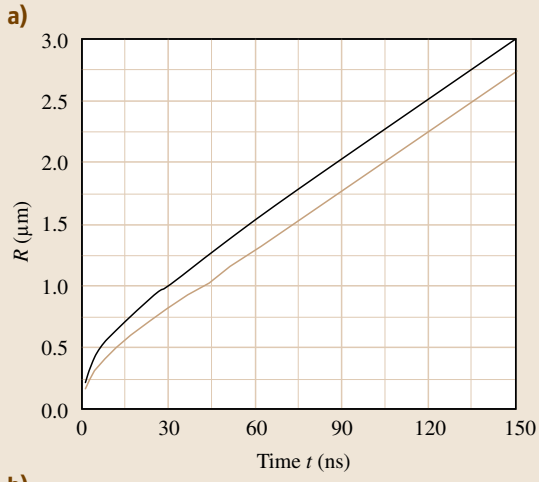

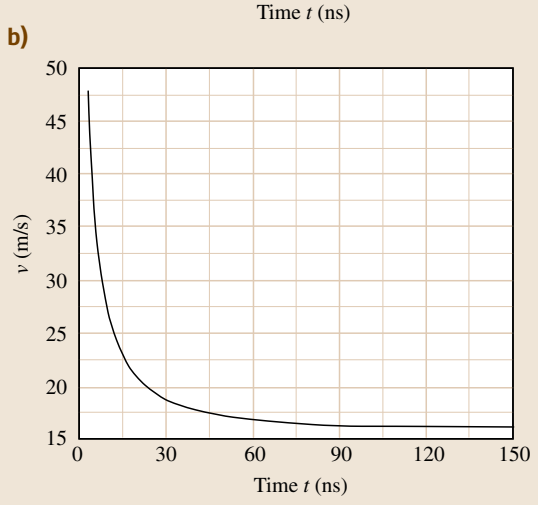

Fig. 30.24 **(a)** Bubble expansion around a 30 nm gold particle in blood irradiated by a laser pulse with energy density $E = 0.33\,\mathrm{J/cm^2}$ and pulse duration $\tau_L = 8\,\mathrm{ns}$ at constant bubble temperature (*upper curve*) and under adiabatic conditions (*lower curve*). **(b)** Bubble expansion rate, $v(t) = \mathrm{d}R/\mathrm{d}t$

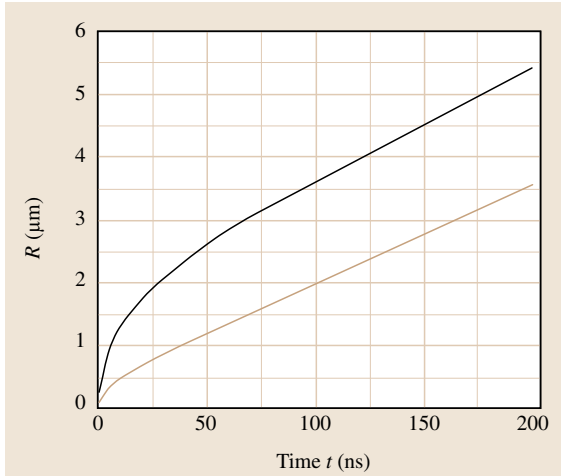

Fig. 30.25 Adiabatic expansion of the bubble produced by a single 30 nm particle (*lower curve*) and 190 nm continuous *cluster* (*upper curve*) irradiated by a laser pulse with energy density $E = 0.33\,\mathrm{J/cm^2}$ and pulse duration $\tau_L = 8\,\mathrm{ns}$

sults [30.12], which include the study of nanocluster-related phenomena as discussed in Sect. 30.5.1 and below.

Microbubble Generation Around Nanoclusters

The model described above has been used to calculate the bubble growth in time around 30 nm gold particles and homogeneous clusters with radius of 190 nm surrounded by blood biomedium when the incident laser pulse has energy density of $E = 0.33\,\mathrm{J/cm^2}$ and pulse duration of $\tau_L = 8\,\mathrm{ns}$. The physical properties of blood used in the calculations are listed in Table 30.13. The results of the simulations are presented in Figs. 30.24 and 30.25. Figure 30.24 illustrates the time behavior of the radius and its rate for the bubble generated around the 30 nm particles heated and cooled in blood. Figure 30.25 demonstrates the difference in the time dynamics of bubble growth caused by the single 30 nm particle and 190 nm homogeneous cluster.

Calculations are performed for both cases at constant bubble temperature ($k = 1$) and for adiabatic conditions ($k = \gamma = 4/3$). Under such conditions, the time dependence of the bubble radius $R(t)$ is a better fit to our experimental results [30.12]. As follows from our calculations, the adiabatic expansion of the bubble provides a final radius of 3.5 μm for the bubble lifetime 200 ns, which agrees well with our experimental observations in [30.12].

The general feature of the simulation results is linear and smooth growth of the bubbles' radius with time when the bubbles' lifetime exceeds 30 ns. The time dynamics of the temperature, as calculated in [30.1] for 30 nm nanoparticles heated by a 8 ns laser pulse, show that the total time for one cycle (heating of the nanoparticles from an initial temperature 300 K to maximum temperature, and then cooling back to the initial temperature) is about 30 ns. Thus, linear growth of the bubble radius with time after 30 ns can be explained by the ab-

sence of an active heat source in the medium. This result is confirmed also by the rate dynamics $v(t) = dR/dt$ for the bubble radius shown in Fig. 30.24b. In the time range 0–30 ns, the curves of both $R(t)$ and $v(t)$ have strong nonlinearity due to active heat transfer from the nanoparticle to the surrounding medium. During the first several nanoseconds, the bubble rapidly expands with a high velocity of 40 m/s. Then, the expansion rate drops exponentially and reaches a constant saturation value of 16 m/s for $t > 30$ ns. Since there is no heating source in the system after 30 ns, the microbubble expands uniformly and linearly at a constant rate.

It is important to compare the bubble expansion rate with the thermal conduction rate in the surrounding medium. Using the thermal properties of blood given in Table 30.13 and the size of the locally heated region $l \approx 1\,\mu$m as a focal spot of the laser radiation, we find that the approximate speed for heat conduction is

$$v_{\text{thermal}} \approx \frac{\mu_0}{\rho c l} \approx 0.15\,\text{m/s}\,, \tag{30.29}$$

which is more than two orders of magnitude less than the bubble expansion rate. Here, ρ, c, and μ_0 are, respectively, the density, specific heat, and thermal conductivity of the surrounding medium. So, during a laser pulse of $\tau_L = 8$ ns, thermal damage occurs over a negligible distance from the nanoparticle in comparison with the bubble damage. Thus, bubble expansion occurs on a time scale much shorter than heat loss, which justifies the use of an adiabatic treatment during the expansion. The thermal relaxation time is 1.75 μs for water and 1.56 μs for blood, which is much longer than the bubble lifetime of about 200 ns. This means that, for cell damage by bubble expansion, it is sufficient to heat only the nanoparticles up to the critical threshold temperature for bubble generation (423 K) without having to heat the surrounding cellular medium. Therefore, the relatively low optical flux of 0.33 J/cm^2 ($\tau_L = 8$ ns) is enough for effective cell killing.

Similar bubble expansion dynamics is observed for the bubble produced by a homogeneous cluster, as illustrated in Fig. 30.25. The cluster's curve has both linear and nonlinear parts with notably higher expansion rate of more than 90 m/s in the first 4 ns. During adiabatic expansion of the bubble produced by a homogeneous cluster in blood, the saturated expansion rate is 17 m/s, and the final radius reaches $\approx 5.5\,\mu$m for bubble lifetime of 200 ns. According to our calculations, the heated 380 nm cluster is able to produce one large bubble in the cell volume, whose damage area is comparable to the size of a cancer cell (10–15 μm in diameter). Thus, the formation of just one large bubble around one large nanocluster aggregated in the cell volume is good enough for cancer cell killing.

In conclusion, the bubble mode of photothermolysis decreases the threshold optical flux to 0.33 J/cm^2 ($\tau_L =$ 8 ns) for cancer cell killing and dramatically increases the damage area due to rapid expanding microbubbles around the nanoparticles and cluster:

- The expansion of the bubble has a strong nonlinearity in the time range 0–30 ns due to active heat transfer from nanoparticles to the surrounding medium. During the first several nanoseconds, the bubble produced around a 30 nm particle rapidly expands with a high velocity of 40 m/s. Then, the expansion rate drops exponentially and reaches a constant saturation value of 16 m/s for $t > 30$ ns. Since there is no heating source in the system after 30 ns, the microbubble expands uniformly and linearly at a constant rate.
- The adiabatic expansion of the bubble produced around a single 30 nm particle reaches a final radius of 3.5 μm for bubble lifetime of 200 ns.
- The speed for heat conduction in the cellular medium ($v_{\text{thermal}} = 0.15$ m/s) is more than two orders of magnitude less than the bubble expansion rate ($v_{\text{saturated}} = 16$ m/s), so that, during a laser pulse of $\tau_L = 8$ ns, thermal damage occurs over a negligible distance from the nanoparticle in comparison with the bubble damage.
- A heated 380 nm cluster is able to produce a single large bubble within the cell volume, whose damage area is comparable to the size of a cancer cell (10–15 μm in diameter).

30.6.3 Laser-Induced Thermal Explosion Mode – Nanobombs

In this section, we discuss a new mechanism for selective laser killing of abnormal cells by laser thermal explosion of single nanoparticles – nanobombs – delivered to the cells. Thermal explosion of the nanoparticles is realized for ultrashort laser pulses when the heat is generated within the strongly absorbing target more rapidly than the heat can diffuse away. Laser-induced rapid explosive evaporation of gold nanoparticles (GNs) enables the generation of stress transients, shock waves, and high local pressure. A schematic picture of these complex physical effects is provided in Figs. 30.26 and 30.27. There are two main physical mechanisms

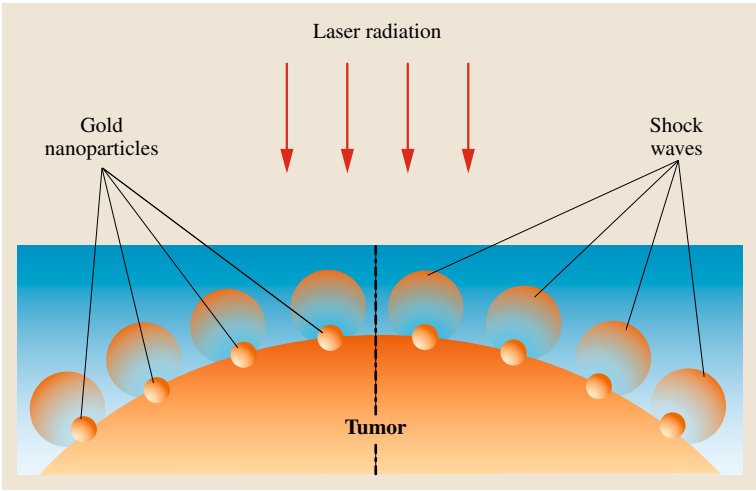

Fig. 30.26 Principle of the thermal explosion mode of nanoparticles – nanobombs – in selective nanophototherolysis of cancer

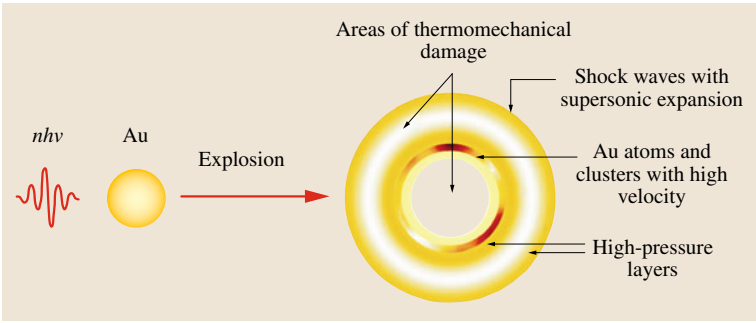

Fig. 30.27 Laser-induced thermal explosion of a gold nanoparticle

that could lead to the laser-induced explosion of GNs: the *thermal explosion mode* through electron–phonon excitation–relaxation, and the *Coulomb explosion mode* through multiphoton ionization.

Thermal Explosion Mode

Under the action of ultrashort laser pulses in the spectral range of the surface plasmon resonances (for a solid spherical GN, the maximum absorption is $\approx 520\,\mathrm{nm}$), GN atoms are excited to upper electronic states owing to the absorption of many photons. Through rapid (picosecond time scale) relaxation, GN atoms decay to their ground state with effective electron–phonon conversion of the absorbed photon energy into thermal energy. Depending on the GN temperature T, the following scenarios, individually or in combination, can occur:

1. $T < T_{\mathrm{LV}}$, where T_{LV} is the liquid vaporization temperature (water in many cases), ≈ 150–$350\,^{\circ}\mathrm{C}$ [30.54]. This is thermal expansion of a single GN and surrounding thin liquid layer, which is accompanied by the generation of linear acoustic waves, known as the *classic* photoacoustic effect.
2. $T_{\mathrm{LV}} \leq T < T_{\mathrm{GNM}}$, where T_{GNM} is the GN melting point, $\approx 1063\,^{\circ}\mathrm{C}$ [30.55]. This is bubble formation with expansion and collapse, which is accompanied by the production of acoustic and shock waves [30.56, 57].
3. $T_{\mathrm{GNM}} \leq T < T_{\mathrm{GNB}}$, where T_{GNB} is the GN boiling point of $\approx 2710\,^{\circ}\mathrm{C}$ [30.55], with GN melting.
4. $T \geq T_{\mathrm{GNB}}$, which is GN boiling with the formation of gold vapor around liquid gold drops.

The photothermal process of scenario 3, and especially scenario 4, may lead to GN fragmentation into smaller parts – nanobullets – and to the thermal explosion of a GN into single atoms.

Coulomb Explosion Mode

For ultrashort laser pulses (e.g., femtosecond time scale) comparable to the time scale of electron–electron

interactions and shorter than the electron–phonon interaction time, a nonphotothermal mechanism of GN explosion can occur through multiphoton ionization when the absorbed photon energy is transferred directly to the electrons, leading to their ejection due to the Coulomb explosion mechanism [30.58, 59]. High GN plasmon-resonance absorption may facilitate this effect due to thermionic electron emission.

Time Scale Approximations

The goal of this theoretical modeling is to estimate the threshold laser energy density E_{expl} required for realization of the thermal explosion mode of GNs, and to compare the calculated data with available experimental results. This mode is realized through rapid overheating of a strongly absorbing target during a short laser pulse when the influence of heat diffusion is minimal. Let us first estimate the time scale for thermal relaxation due to heat diffusion from the surface of the nanoparticle.

In the vicinity of GN $\leq 5R$, where R is the nanoparticle's radius, the thermal relaxation time for a spherical GN can be estimated as $\tau_{\mathrm{T}} = R^2/6.75k$, where k is the thermal diffusivity [30.1]. For $R = 50$, 100, and 200 nm, estimates of τ_{T} (for water, $k = 1.44\times10^{-3}\,\mathrm{cm^2/s}$) are approximately 2.6, 10, and 41 ns, respectively. For a laser pulse duration $t_{\mathrm{P}} \leq \tau_{\mathrm{T}}$, heat is generated within the GN more rapidly than it can be diffused away, so that we can neglect heat losses from the surface of the GN due to heat diffusion into the surrounding medium. This condition for smaller GNs is valid with picosecond and femtosecond laser pulses.

Threshold Intensity for Laser-Induced Thermal Explosion

Consider a nanoparticle selectively delivered to a targeted site (e.g., cancer cell) to be irradiated by a laser of intensity I. The power of the absorbed electromagnetic field is $P = \sigma_{\mathrm{abs}} I$, where σ_{abs} is the GN's cross-section of absorption. If σ_{abs} is large enough, thermal explosion of the GN may occur at certain values of the threshold laser intensity I_{expl}, which is less than the threshold intensity for optical plasma formation in the surrounding medium [30.17, 18]. Under the thermal explosion of GNs, we understand the specific case for which the total energy absorbed by the GN during the time of its inertial retention in vapor state, $\tau_{\mathrm{expl}} = R/u_{\mathrm{s}}$, exceeds the energy required for the GN's complete evaporation, $\rho q V = N_{\mathrm{Au}} q_1 V$. Here, u_{s} is the sound velocity in Au vapor at the critical temperature $T_{\mathrm{cr}} \sim T_{\mathrm{GNB}}$; ρ is the volume density of GN; N_{Au} is the number of Au atoms per unit volume; q and q_1 are the particle's specific heat of evaporation per unit mass and per particle, respectively; and V is the GN's volume. We have a laser pulse duration of $\tau_{\mathrm{L}} > \tau_{\mathrm{expl}} = R/u_{\mathrm{s}}$ (≈ 1 ps for $R \approx 10$ nm), where τ_{expl} is an explosive evaporation time.

To compute I_{expl}, we can use the model described in [30.1]. According to that model, the threshold intensity of the laser radiation for thermal explosion of the spherical GN can be expressed as

$$I_{\mathrm{expl}}(R) \approx \frac{4\rho T_{\mathrm{cr}} q u_{\mathrm{s}}}{3K_{\mathrm{abs}}(R)}\,, \tag{30.30}$$

where K_{abs} is the nanoparticle absorption efficiency. Thus, the solid nanoparticle in a relatively strong laser field with intensity $I \geq I_{\mathrm{expl}}$ during the short time $\tau_{\mathrm{expl}} \approx R/u_{\mathrm{s}}$ transforms into a gas (vapor) sphere of radius $\approx R$, which has high temperature $T \sim T_{\mathrm{GNB}}$ and high pressure $P_{\mathrm{vap}} \gg P_{\infty}$, where P_{∞} is the ambient pressure.

We assume here that thermal explosion of a GN is accompanied by the generation of shock waves that expand with a supersonic velocity $u_{\mathrm{s}} = R/\tau_{\mathrm{expl}} = I_{\mathrm{expl}}/4\Delta H \approx 10^5\,\mathrm{cm/s}$. Here, $\Delta H = \Delta H_{300-\mathrm{vap}} + \Delta H_{\mathrm{vap}}$, where $\Delta H_{300-\mathrm{vap}}$ is the enthalpy change per unit volume for heating the GN from the ambient temperature to the vaporization temperature, and ΔH_{vap} is the vaporization enthalpy per unit volume. The shock waves could be waves of high acoustic or/and water vapor pressure, which spread out over long distances around an epicenter of explosion and produce irreparable mechanical cell damage [30.60–67]. It should be noted that the pressure produced by vaporization of a GN itself (e.g., $\approx 10^{-2}$ atm [30.68]) is less than the water vapor pressure around the hot GNs. Indeed, the number of atoms vaporized per unit of time and per unit of particle surface is given by [30.69]

$$\frac{\mathrm{d}N_{\mathrm{vap}}}{\mathrm{d}t} = u_{\mathrm{s}} N_{\mathrm{Au}} = \frac{I_{\mathrm{expl}}}{4\Delta H} N_{\mathrm{Au}}\,. \tag{30.31}$$

For example, the atomic density of bulk gold is $5.9\times10^{22}\,\mathrm{cm^{-3}}$, while each GN contains approximately 10^9 atoms, leading to an average atom density of $10^{17}\,\mathrm{cm^{-3}}$. Higher gold vapor pressure can only be reached on the front end of the explosion, where explosion products are localized in a thin layer.

Cell Damage Effects

The therapeutic effect of laser-induced explosion of GNs for cancer treatments can be achieved due to one or several phenomena, such as protein inactivation (e.g., through denaturation or coagulation) around hot GNs [30.61], bubble formation [30.12], generation of

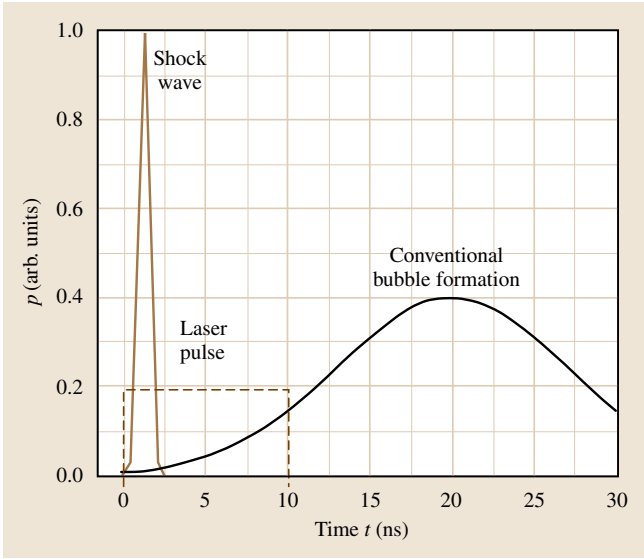

Fig. 30.28 Schematic time scale for shock wave and conventional bubble formation using the thermal explosion mode

acoustic and shock waves [30.62–67], and interaction with GN fragments and atoms. An important damage-related factor is not only the temperature but also the vapor pressure produced by both water and gold vapors, accompanied by the cavitations and shock waves, with local pressure up to gigapascals [30.62–67]. The damage of specific cellular structures (e.g., plasmatic membranes, nuclei, cytoskeletons, and organelles) in the laser explosion mode depends on GN parameters (composition, size, and shape), their number and location, laser parameters (wavelength, fluence, pulse duration, and number of pulses), and properties of the surrounding media (e.g., amount of water).

The time required to destroy an abnormal cell of size d by supersonic expansion of shock waves can be roughly estimated as $\tau_{sw} \approx d/u_s$. In the case of 15 μm-diameter cancer cells [30.12, 17, 18], this is $\tau_{sw} \approx 15$ ns, which is comparable to the lifetime of sound/pressure shock waves in an aqueous medium. We can estimate the lower level of the threshold energy density of a laser pulse required for thermal explosion of the GN using $E_{expl}(R) \approx I_{expl}(R) \times \tau_{expl}$, where the threshold intensity I_{expl} depends on the absorption efficiency of the nanoparticle. For the particular lasers used in the experiments [30.12, 17, 18] ($\lambda = 532$ nm, $\tau_L = 8–10$ ns), the threshold energy density for thermal explosion of a solid gold nanosphere of size $R = 35$ nm (absorption efficiency of $K_{abs} = 4.02$) is $E_{expl} = 38.5\,\mathrm{mJ/cm^2}$. This density strongly depends on the types of nanoparticles (e.g., gold solid nanospheres, nanoshells, and nanorods). For example, gold nanorods have a near-IR resonance absorption efficiency of approximately 14 for an effective radius of 11.43 nm [30.26]. Due to the higher plasmon-resonance absorption efficiency of nanorods, the threshold energy density can be reduced by using gold nanorods to $E_{expl} = 25\,\mathrm{mJ/cm^2}$. It is important to note that the estimated threshold energy densities for thermal explosion of GNs at the given wavelength $\lambda = 532$ nm are 2.5–4 times less than the laser fluence of $100\,\mathrm{mJ/cm^2}$ established as the safety standard for medical lasers [30.70].

The estimated values for E_{expl} are in good agreement with some available experimental results. Indeed, for spherical GNs with average size of 45 nm irradiated with second-harmonic Nd:YAG laser pulses (532 nm for 7 ns), the laser fluence threshold for changing the GN shape and its fragmentation associated with GN melting and boiling phenomena are 16 and $30\,\mathrm{mJ/cm^2}$, respectively [30.55]. The more intense GN fragmentation to small fragments of mainly 5–10 nm in size has been observed for laser fluences in the range $30–140\,\mathrm{mJ/cm^2}$ and higher [30.55]. For a 30 ps pulse, 25 nm GN fragmentation has been observed at $23\,\mathrm{mJ/cm^2}$, with a slight effect on changing the GN shape, even at $2–5\,\mathrm{mJ/cm^2}$ [30.28].

Thus, thermal explosion around GNs may make a significant contribution to cell damage alone or together with conventional water vapor bubble formation in nanophotothermolysis, which is characterized by a higher laser fluence range of $50–500\,\mathrm{mJ/cm^2}$ [30.1]. As previously mentioned, conventional bubble formation usually starts at the end of a nanosecond laser pulse, while the thermal explosion time scale is from 1 ps to a few ns [30.17, 18]. A schematic time scale for shock wave and conventional bubble formation in the thermal explosion mode is shown in Fig. 30.28. Thus, shock waves appear earlier than bubbles induced by the explosive vaporization of GNs in a liquid environment.

The laser-induced explosion effect can explain the experimental results [30.7, 16] with notable cancer damage with 1.4 nm GNs inside viruses on a cell membrane with picosecond laser pulses (30 ps, $50–100\,\mathrm{mJ/cm^2}$) when the probability of classic water bubble formation is very low. We believe that the explosion mode may be essential in selective nanophotothermolysis of DNA, and this mode is definitely becoming dominant in the absence of a sufficient amount of water around GNs. This mode can be combined with a bubble overlapping

mode [30.12] as described above, where the explosion of a few closely located GNs in a gold nanoparticle cluster (GNC) can produce one large bubble with enhanced killing efficiency. The explosion of GNs on smaller particles or single gold atoms during a laser pulse may provide the condition for interaction of the pulse with its atoms, leading to their ionization and plasma formation. However, these effects should appear at relatively high laser fluences that are not safe for normal cells [30.57].

Thus, we have considered a new mechanism for selective laser killing of abnormal cells by laser thermal explosion of single nanoparticles (nanobombs) delivered to the cells. Thermal explosion is realized when heat is generated within a strongly absorbing target more rapidly than the heat can diffuse away. On the basis of simple energy balance, it is shown that the threshold energy density of a single laser pulse required for the thermal explosion of a solid gold nanosphere is approximately 40 mJ/cm^2. The nanoparticle's explosion threshold energy density can be reduced further (to 11 mJ/cm^2) by using large nanorods (and probably nanoshells) and many other advanced GNs whose optical plasmon resonance lies in the near-IR region, where the biological tissue transmissivity is the highest. Additionally, the effective therapeutic effect for cancer cell killing is achieved due to nonlinear phenomena that accompany the thermal explosion of the nanoparticles, such as the generation of GN explosion products with high kinetic energy (nanobullets), as well as strong shock waves with supersonic expansion in the cell volume or production of optical plasma. It is important that most of these phenomena can explain some published experimental results whose interpretation was performed without taking into account this effect.

References

30.1 T.F. George, D. Jelski, R.R. Letfullin, G. Zhang (Eds.): *Computational Studies of New Materials II: From Ultrafast Processes and Nanostructures to Optoelectronics, Energy Storage and Nanomedicine* (World Scientific, Singapore 2011)

30.2 T.M. Fahmy, P.M. Fong, A. Goyal, W.M. Saltzman: Targeted for drug delivery, Nano Today, August 18–26 (2005)

30.3 Y. Fukumori, H. Ichikawa: Nanoparticles for cancer therapy and diagnosis, Adv. Powder Technol. **17**, 1–28 (2006)

30.4 S. Nie, Y. Xing, G.J. Kim, J.W. Simons: Nanotechnology applications in cancer, Annu. Rev. Biomed. Eng. **9**, 257–288 (2007)

30.5 R.R. Letfullin, V.I. Igoshin, A.N. Bekrenev: Thermal calculation of bone-tissue slash modes by laser radiation, Proc. SPIE **2100**, 272–275 (1994)

30.6 R.R. Letfullin, V.P. Zharov, C. Joenathan, T.F. George: Nano-photothermolysis of cancer cells, SPIE Newsroom (2007)

30.7 V.P. Zharov, K.E. Mercer, E.N. Galitovskaya, M.S. Smeltzer: Photothermal nanotherapeutics and nanodiagnostics for selective killing of bacteria targeted with gold nanoparticles, Biophys. J. **90**, 619–627 (2006)

30.8 G.A. Mansoori, P. Mohazzabi, P. McCormack, S. Jabbari: Nanotechnology in cancer prevention, detection, and treatment: Bright future lies ahead, World Rev. Sci. Technol. Sustain. Dev. **4**, 226–257 (2007)

30.9 C.M. Pitsillides, E.K. Joe, X. Wei, R.R. Anderson, C.P. Lin: Selective cell targeting with light-absorbing microparticles and nanoparticles, Biophys. J. **84**, 4023–4032 (2003)

30.10 M.J. Vicent: Polymer-drug conjugates as modulators of cellular apoptosis, Am. Assoc. Pharm. Sci. J. **9**, E200–E207 (2007)

30.11 J. Khandare, T. Minko: Polymer-drug conjugates: progress in polymeric prodrugs, Prog. Polym. Sci. **31**, 359–397 (2006)

30.12 V.P. Zharov, R.R. Letfullin, E.N. Galitovskaya: Microbubbles-overlapping mode for laser killing of cancer cells with absorbing nanoparticle clusters, J. Phys. D **38**, 2571–2581 (2005)

30.13 J.R. Lepock, H.E. Frey, K.P. Ritchie: Protein denaturation in intact hepatocytes and isolated cellular organelles during heat shock, J. Cell Biol. **122**, 1267–1276 (1993)

30.14 C. Yao, R. Rahmanzadeh, E. Endl, Z. Zhang, J. Gerdes, G. Hüttmann: Elevation of plasma membrane permeability by laser irradiation of selectively bound nanoparticles, J. Biomed. Opt. **10**, 064012–1–064012–8 (2005)

30.15 R.R. Letfullin, C.E.W. Rice, T.F. George: Bone tissue heating and ablation by short and ultrashort laser pulses, Proc. SPIE **7548**, 75484K–1–75484K–11 (2010)

30.16 R.R. Letfullin, T.F. George: Laser ablation of biological tissue by short and ultrashort pulses. In: *Computational Studies of New Materials II*, ed. by T.F. George, D. Jelski, R.R. Letfullin, G.P. Zhang (World Scientific, Singapore 2011) pp. 191–218

30.17 R.R. Letfullin, C. Joenathan, T.F. George, V.P. Zharov: Laser-induced explosion of gold nanoparticles: Potential role for nanophotothermolysis of cancer, Nanomedicine **1**, 473–480 (2006)

30.18 R.R. Letfullin, V.P. Zharov, C. Joenathan, T.F. George: Laser-induced thermal explosion mode for selec-

tive nano-photothermolysis of cancer cells, Proc. SPIE **6436**, 643601–1–643601–5 (2007)
30.19 R.R. Letfullin, C.E.W. Rice, T.F. George: Space simulation of thermal fields generated in bone tissue for application to nanophotohyperthermia and nanophotothermolysis, Proc. SPIE **7883**, 78834–L–1–78834–L–10 (2011)
30.20 R.R. Letfullin, T.F. George, G.C. Duree, B.M. Bollinger: Ultrashort laser pulse heating of nanoparticles: Comparison of theoretical approaches, Adv. Opt. Technol. **2008**, 251718–1–251718–8 (2008)
30.21 R.R. Letfullin, T.F. George: Nanomaterials in nanomedicine. In: *Computational Studies of New Materials II: From Ultrafast Processes and Nanostructures to Optoelectronics, Energy Storage and Nanomedicine*, ed. by T.F. George, D. Jelski, R.R. Letfullin, G.P. Zhang (World Scientific, Singapore 2011) pp. 103–130
30.22 R.R. Letfullin, T.F. George: New dynamic modes for selective laser cancer nanotherapy. In: *Computational Studies of New Materials II: From Ultrafast Processes and Nanostructures to Optoelectronics, Energy Storage and Nanomedicine*, ed. by T.F. George, D. Jelski, R.R. Letfullin, G.P. Zhang (World Scientific, Singapore 2011) pp. 131–172
30.23 R.R. Letfullin, C.E.W. Rice, T.F. George: Modeling photothermal heating and ablation of biological hard tissues by short and ultrashort laser pulses, Int. J. Theor. Phys. Group Theor. Nonlinear Opt. **15**, 11–23 (2011)
30.24 R.R. Letfullin, C.B. Iversen, T.F. George: Modeling nanophotothermal therapy: Kinetics of thermal ablation of healthy and cancerous cell organelles and gold nanoparticles, Nanomedicine **7**(2), 137–145 (2011)
30.25 R.R. Letfullin, T.F. George: Nanoscale materials in strong ultrashort laser fields. In: *Computational Studies of New Materials II: From Ultrafast Processes and Nanostructures to Optoelectronics, Energy Storage and Nanomedicine*, ed. by T.F. George, D. Jelski, R.R. Letfullin, G.P. Zhang (World Scientific, Singapore 2011) pp. 37–64
30.26 P.K. Jain, K.S. Lee, I.H. El-Sayed, M.A. El-Sayed: Calculated absorption and scattering properties of gold nanoparticles of different size, shape, and composition: Applications in biological imaging and biomedicine, J. Phys. Chem. B **110**, 7238–7248 (2006)
30.27 V.K. Pustovalov, A.S. Smetannikov, V.P. Zharov: Photothermal and accompanied phenomena of selective nanophotothermolysis with gold nanoparticles and laser pulses, Laser Phys. Lett. **5**, 775–792 (2008)
30.28 Z. Peng, T. Walther, K. Kleinermanns: Influence of intense pulsed laser irradiation on optical and morphological properties of gold nanoparticle aggregates produced by surface acid–base reactions, Langmuir **21**, 4249–4253 (2005)
30.29 V.S. Kalambur, E.K. Longmire, J.C. Bischof: Cellular level loading and heating of superparamagnetic iron oxide nanoparticles, Langmuir **23**, 12329–12336 (2007)
30.30 E.Y. Hleb, D.O. Lapotko: Photothermal properties of gold nanoparticles under exposure to high optical energies, Nanotechnology **19**, 1–10 (2008)
30.31 H. Takahashi, T. Niidome, A. Nariai, Y. Niidome, S. Yamada: Gold nanorod-sensitized cell death: Microscopic observation of single living cells irradiated by pulsed near-infrared laser light in the presence of gold nanorods, Chem. Lett. **35**, 500–501 (2006)
30.32 P. Buffat, J.P. Borel: Size effect on the melting temperature of gold particles, Phys. Rev. A **13**, 2287–2298 (1976)
30.33 T. Torimura, T. Ueno, S. Inuzuka, Y. Kimura, P. Ko, M. Kin, T. Minetoma, T. Majima, M. Sata, H. Abe, K. Tanikawa: Ultrastructural observation on hepatocellular carcinoma: Correlation of tumor grade and degree of atypia of cell organelles by morphometry, Med. Electron. Microsc. **26**, 19–28 (1993)
30.34 G.T. Deans, P.W. Hamilton, P.C.H. Watt, M. Heatly, K. Williamson, C.C. Patterson, B.J. Rowlands, G. Parks, R. Spence: Morphometric analysis of colorectal cancer, Dis. Colon Rectum **36**, 450–456 (1993)
30.35 M.M. Radwan, K.A. Amer, N.M. Mokhtar, M.A. Kandil, A.M. El-Barbary, H.A. Aiad: Nuclear morphometry in ductal breast carcinoma with correlation to cell proliferative activity and prognosis, J. Egypt. Natl. Cancer Inst. **15**, 169–182 (2003)
30.36 D. Ozaki, Y. Kondo: Comparative morphometric studies of benign and malignant intraductal proliferative lesions of the breast by computerized image analysis, Hum. Pathol. **26**, 1109–1113 (1995)
30.37 Y. Cui, E.A. Koop, P.J. van Diest, R.A. Kandel, T.E. Rohan: Nuclear morphometric features in benign breast tissue and risk of subsequent breast cancer, Breast Cancer Res. Treat. **104**, 103–107 (2007)
30.38 N. Campbell, J. Reece: *The Cell: A Tour of the Cell Biology*, 8th edn. (Benjamin Cummings, San Francisco 2007)
30.39 M. Bloom, J. Greenbeerg (Eds.): *BSCS Biology, A Molecular Approach, BSCS Blue Version*, 9th edn. (Glencoe/McGraw-Hill, Columbus 2006)
30.40 D.E. Sadava: *Cell Biology: Organelle Structure and Function* (Jones Bartlett, Boston 1993)
30.41 L.W. Anson, R.C. Chivers: Ultrasonic propagation in mammalian cell suspensions based on a shell model, Phys. Med. Biol. **34**, 1153–1167 (1989)
30.42 D.L. Martin, J. Sampugna: Stimulating Cell Fractionation (Carolina Biological Supply Company 1973), pp. 50–51
30.43 H. Goldenberg, C.J. Tranter: Heat flow in an infinite medium heated by a sphere, Br. J. Appl. Phys. **3**, 296–298 (1952)

30.44 S.R.H. Davidson, D.F. James: Measurement of thermal conductivity of bovine cortical bone, Med. Eng. Phys. **22**, 741–747 (2000)

30.45 P.L. Blanton, N.L. Biggs: Density of fresh and embalmed human compact and cancellous bone, Am. J. Phys. Anthropol. **29**, 39–44 (1968)

30.46 H. Fukushima, Y. Hashimoto, S. Yoshiya, M. Kurosaka, M. Matsuda, S. Kawamura, T. Iwatsubo: Conduction analysis of cement interface temperature in total knee arthroplasty, Kobe J. Med. Sci. **48**, 63–72 (2002)

30.47 A. Shakeri-Zadeh, M. Ghasemifard, G.A. Mansoori: Structural and optical characterization of folateconjugated gold-nanoparticles, Physica E **42**, 1272–1280 (2010)

30.48 P.B. Johnson, R.W. Christy: Optical properties of the noble metals, Phys. Rev. B **6**, 4370–4379 (1972)

30.49 D. Fried, M. Zuerlein, J.D.B. Featherstone, W. Seka, C. Duhn, S.M. McCormack: IR laser ablation of dental enamel: Mechanistic dependence on the primary absorber, Appl. Surf. Sci. **127–129**, 852–856 (1998)

30.50 M.C. Daniel, D. Astruc: Gold nanoparticles: Assembly, supramolecular chemistry, quantum-size-related properties and application toward biology, catalysis and nanotechnology, Chem. Rev. **104**, 293–346 (2004)

30.51 C.P. Lin, M.W. Kelly, S.A. Sibayan, M.A. Latina, R.R. Anderson: Selective cell killing by microparticle absorption of pulsed laser radiation, IEEE J. Sel. Top. Quantum Electron. **5**, 963–968 (1999)

30.52 C.E. Brennen: *Cavitation and Bubble Dynamics* (Oxford Univ. Press, New York 1995)

30.53 K. Aslan, J.R. Lakowicz, C.D. Geddes: Nanogold-plasmon-resonance-based glucose sensing, Anal. Biochem. **330**, 145–155 (2004)

30.54 J. Neumann, R. Brinkmann: Boiling nucleation on melanosomes and microbeads transiently heated by nanosecond and microsecond laser pulses, J. Biomed. Opt. **10**, 024001–024012 (2005)

30.55 A. Takami, H. Kurita, S. Koda: Laser-indiced size reduction of noble particle, J. Phys. Chem. B **103**, 1226–1232 (1999)

30.56 R.R. Anderson, J.A. Parrish: Selective photothermolysis: Precise microsurgery by selective absorption of pulsed radiation, Science **220**, 524–527 (1983)

30.57 V. Venugopalan, A. Gyerra III, K. Nahen, A. Vogel: Role of laser-induced plasma formation in pulsed cellular microsurgery and micromanipulation, Phys. Rev. Lett. **88**, 078103–1–078103–4 (2002)

30.58 A. Vogel, V. Venugolapan: Mechanism of pulsed laser ablation of biological tissue, Chem. Rev. **103**, 577–644 (2003)

30.59 K. Yamada, Y. Tokumoto, T. Nagata, F. Mafune: Mechanism of laser-induced size-reduction of gold nanoparticles as studied by nanosecond transient absorption spectroscopy, J. Phys. Chem. B **110**, 11751–11756 (2006)

30.60 S. Inasawa, M. Sugiyama, S. Noda, Y. Yamaguchi: Spectroscopic study of laser-induced phase transition of gold nanoparticles on nanosecond time scale and longer, J. Phys. Chem. B **110**, 3114–3119 (2006)

30.61 G. Huttmann, B. Radt, J. Serbin, R. Birngruber: Inactivation of proteins by irradation of gold nanoparticles with nano- and picosecond laser pulses, Proc. SPIE **5142**, 88–95 (2003)

30.62 P. Steinbach, F. Hofstadter, H. Nicolai, W. Rossier, W. Wieland: In vitro investigations on cellular damage induced by high energy shock waves, Ultrasound Med. Biol. **18**, 691–699 (1992)

30.63 A.G. Doukas, D.J. McAuliffe, T.J. Flotte: Biological effects of laser-induced shock waves: Structural and functional cell damage in vitro, Ultrasound Med. Biol. **19**, 137–146 (1993)

30.64 T. Douki, S. Lee, K. Dorey, T.J. Flotte, T.F. Deutsch, A.G. Doukas: Stress-wave-induced injury to retinal pigment epithelium cells in vitro, Lasers Surg. Med. **19**, 249–259 (1996)

30.65 T. Kodama, H. Uenohara, K. Takayama: Innovative technology for tissue disruption by explosive-induced shock waves, Ultrasound Med. Biol. **24**, 1459–1466 (1998)

30.66 A. Sonden, B. Svensson, N. Roman, H. Ostmark, B. Brismar, J. Palmblad, B.T. Kjellstrom: Laser-induced shock wave endothelial cell injury, Lasers Surg. Med. **26**, 364–375 (2000)

30.67 E. Faraggi, B.S. Gerstman, J. Sun: Biophysical effects of pulsed lasers in the retina and other tissues containing strongly absorbing particles: Shockwave and explosive bubble generation, J. Biomed. Opt. **10**, 064029–1–064029–10 (2005)

30.68 S. Inasawa, M. Sugiyama, Y. Yamaguchi: Bimodal size distribution of gold nanoparticles under picosecond laser pulses, J. Phys. Chem. B **109**, 9404–9410 (2005)

30.69 L. Boufendi, A. Bouchoule, B. Dubreuil, E. Stoffels, W.W. Stoffels, M.L. deGiorgi: Study of initial dust formation in an Ar-SiH_4 discharge by laser induced particle explosive evaporation, J. Appl. Phys. **76**, 148–153 (1994)

30.70 ANSI Standard Z136.1-2000: American National Standard for safe use of Lasers ANSIZ136.1 (2000)